

# Physics-informed Deep Diffusion MRI Reconstruction with Synthetic Data: Break Training Data Bottleneck in Artificial Intelligence

Chen Qian<sup>1</sup>, Yuncheng Gao<sup>1</sup>, Mingyang Han<sup>1</sup>, Zi Wang<sup>1</sup>, Dan Ruan<sup>1</sup>, Yu Shen<sup>2</sup>, Yiping Wu<sup>2</sup>, Yirong Zhou<sup>1</sup>, Chengyan Wang<sup>3</sup>, Boyu Jiang<sup>4</sup>, Ran Tao<sup>4</sup>, Zhigang Wu<sup>5</sup>, Jiazheng Wang<sup>5</sup>, Lihong Zhu<sup>6</sup>, Yi Guo<sup>6</sup>, Taishan Kang<sup>7</sup>, Jianzhong Lin<sup>7</sup>, Tao Gong<sup>8</sup>, Chen Yang<sup>9</sup>, Guoqiang Fei<sup>10</sup>, Meijin Lin<sup>11</sup>, Di Guo<sup>12</sup>, Jianjun Zhou<sup>6</sup>, Meiyun Wang<sup>2,13</sup>, and Xiaobo Qu<sup>1\*</sup>

**Abstract:** Diffusion magnetic resonance imaging (MRI) is the only imaging modality for non-invasive movement detection of in vivo water molecules, with significant clinical and research applications. Diffusion MRI (DWI) acquired by multi-shot techniques can achieve higher resolution, better signal-to-noise ratio, and lower geometric distortion than single-shot, but suffers from inter-shot motion-induced artifacts. These artifacts cannot be removed prospectively, leading to the absence of artifact-free training labels. Thus, the potential of deep learning in multi-shot DWI reconstruction remains largely untapped. To break the training data bottleneck, here, we propose a Physics-Informed Deep DWI reconstruction method (PIDD) to synthesize high-quality paired training data by leveraging the physical diffusion model (magnitude synthesis) and inter-shot motion-induced phase model (motion phase synthesis). The network is trained only once with 100,000 synthetic samples, achieving encouraging results on multiple realistic in vivo data reconstructions. Advantages over conventional methods include: (a) Better motion artifact suppression and reconstruction stability; (b) Outstanding generalization to multi-scenario reconstructions, including multi-resolution, multi-b-value, multi-undersampling, multi-vendor, and multi-center; (c) Excellent clinical adaptability to patients with verifications by seven experienced doctors ( $p < 0.001$ ). In conclusion, PIDD presents a novel deep learning framework by exploiting the power of MRI physics, providing a cost-effective and explainable way to break the data bottleneck in deep learning medical imaging.

**Teaser:** Physical-informed, synthetic data, deep learning, diffusion MRI, image reconstruction.

Deep learning (DL) has made significant achievements in many biomedical magnetic resonance imaging (MRI) tasks<sup>1-4</sup>. A large amount of paired training data is commonly required for supervised training<sup>1,5</sup>. For example, in fast imaging<sup>6,7</sup>, fully sampled scanner data (also called k-space) and its undersampled one are routinely employed as paired labels and inputs<sup>6,7</sup>. However, high-quality paired data is absent or insufficient in many MRI scenarios<sup>8,9</sup>, resulting in a training data bottleneck in DL image reconstructions<sup>10</sup>. One representative example is the high-resolution diffusion MRI (DWI)<sup>11-14</sup>.

DWI can detect the *in vivo* water molecule movements non-invasively<sup>15</sup>. It has been widely employed in tumor and stroke diagnosis<sup>16-18</sup> and tissue microstructure research<sup>19</sup>. Multi-shot interleaved echo planar imaging (ms-iEPI) sequence can obtain DWI with higher resolution, better signal-to-noise ratio, and lower geometric distortion<sup>12,20-23</sup>. However, during each shot of data acquisition, the subject motion is different. Even slight subject movement on the millimeter scale will cause the significant extra inter-shot phase (motion phase) to be enlarged by strong diffusion gradients<sup>24</sup>, resulting in severe image motion artifacts<sup>25,26</sup>. The physical movement is hardly detectable<sup>22</sup>, thus the motion artifacts cannot be removed prospectively. Therefore,

the ground truth is absent in multi-shot DWI.

Bypassing the problem of data bottleneck but not solving it, current DL methods acquire a large amount of realistic DWI data and use conventional optimization methods to generate training labels<sup>9,13,27</sup>. Many state-of-the-art optimization methods are developed to reconstruct multi-shot DWI, such as MUSE<sup>22</sup>, MUSSELS<sup>28,29</sup>, and PAIR<sup>30</sup>. Some of them are employed for training label generation and obtain promising results<sup>9,27</sup>. However, these algorithms are hard to recover the high-order motion phases because of the smoothness assumptions on phases<sup>28-30</sup>. For example, PAIR and MUSSELS perform well on synthetic data with the 3-order phase, but failed on the 5-order phase (Figs. 1(m) and (o)).

Thus, training with realistic data or reconstructed labels by optimization methods has several drawbacks, hindering the potential power of DL: (a) Labels contain no or inaccurate high-order motion phases; (b) Sizeable realistic database is hard to be acquired due to long acquisition and reconstruction time, limited budget and ethic constraints; (c) Generalization of current DL methods is poor for reconstructions of multi-scenario, such as multi-resolution, multi-b-value, multi-undersampling, and multi-vendor (Fig. 5).

<sup>1</sup>Department of Electronic Science, Fujian Provincial Key Laboratory of Plasma and Magnetic Resonance, National Institute for Data Science in Health and Medicine, Institute of Artificial Intelligence, Xiamen University, China. <sup>2</sup>Department of Medical Imaging, Henan Provincial People's Hospital & the People's Hospital of Zhengzhou University, China. <sup>3</sup>Human Phenome Institute, Fudan University, China. <sup>4</sup>United Imaging Healthcare, China. <sup>5</sup>Philips Healthcare, China. <sup>6</sup>Department of Radiology, Zhongshan Hospital, Fudan University (Xiamen Branch), China. <sup>7</sup>Department of Radiology, Zhongshan Hospital Affiliated to Xiamen University, China. <sup>8</sup>Departments of Radiology, Shandong Provincial Hospital Affiliated to Shandong First Medical University, China. <sup>9</sup>Department of Neurosurgery, Zhongshan Hospital, Fudan University (Xiamen Branch), China. <sup>10</sup>Department of Neurology, Zhongshan Hospital, Fudan University, China. <sup>11</sup>Department of Applied Marine Physics and Engineering, Xiamen University, China. <sup>12</sup>School of Computer and Information Engineering, Xiamen University of Technology, China. <sup>13</sup>Biomedical Research Institute, Henan Academy of Sciences. Correspondence should be addressed to Xiaobo Qu ([quxiaobo@xmu.edu.cn](mailto:quxiaobo@xmu.edu.cn)).

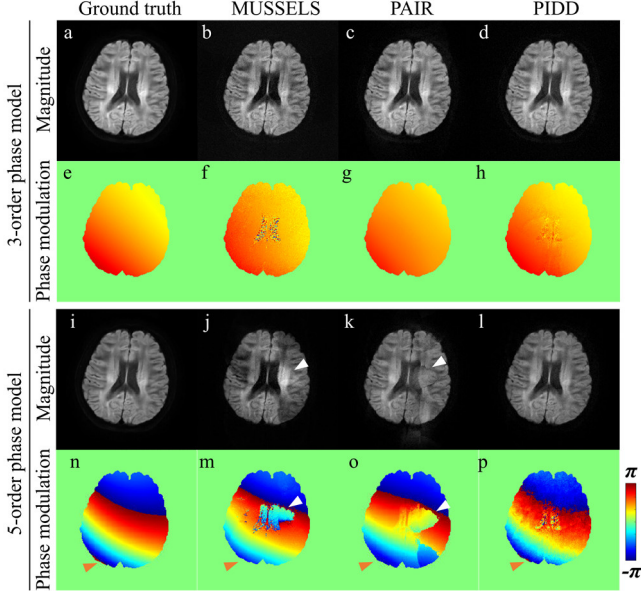


**Fig 1 | Comparison of conventional optimization methods (MUSSELS and PAIR) and the proposed PIDD on synthetic data with 3-order and 5-order motion phases.** The magnitude and phase modulation between the two shots are shown. PIDD is trained with 100,000 synthetic samples with 5-order motion phases. Incorrect and missing motion phases of MUSSELS and PAIR are marked with white and yellow arrows, respectively.

To overcome the fundamental limitation on high-quality training data, we employ an emerging and promising DL paradigm<sup>31,32</sup>, the physics-informed synthetic data training<sup>32</sup>. Following the physical mechanism, it provides high-quality

training data without or with a few real data and has achieved promising performance in biomedical MRI applications<sup>33-36</sup>.

Here, we propose a Physics-Informed Deep Diffusion MRI reconstruction (PIDD). PIDD has two main components (Fig. 2): The physics-informed data synthesis for ms-iEPI DWI (Fig. 2a) and a DL reconstruction network (Fig. 2b). The whole data synthesis process includes: (1) Synthesize DWI magnitude images with specific b-values and diffusion directions according to a physical diffusion model; (2) Synthesize motion phase with an analytically polynomial phase model; (3) Multiply magnitude images with synthetic motion phases to get multi-shot images; (4) Multiply each shot of image with a realistic coil sensitivity; (5) Transform each shot of image of each channel into k-space as the ground truth (label) for network training; (6) Generate network inputs by sampling the noisy k-space.

In the following, we first report data synthesis for magnitude images and motion phases, respectively.

The DWI magnitude is generated according to a physical diffusion model<sup>35</sup>. Here, we choose the diffusion tensor imaging (DTI) model<sup>37</sup>:

$$\mathbf{m}(\mathbf{g}, b) = \mathbf{m}_0 \cdot \exp\{-b\mathbf{g}\mathbf{D}\mathbf{g}^T\}, \quad (1)$$

where  $\mathbf{m}(\mathbf{g}, b)$  is the magnitude of the diffusion signal with diffusion direction  $\mathbf{g}$  and b-value  $b$ , and  $\mathbf{m}_0$  is a non-diffusion image (b-value=0). The  $\mathbf{D}$  is the diffusion tensors. The superscript T is the transpose. Once the high-quality diffusion tensors  $\mathbf{D}$  and  $\mathbf{m}_0$  are known, and imaging experiment

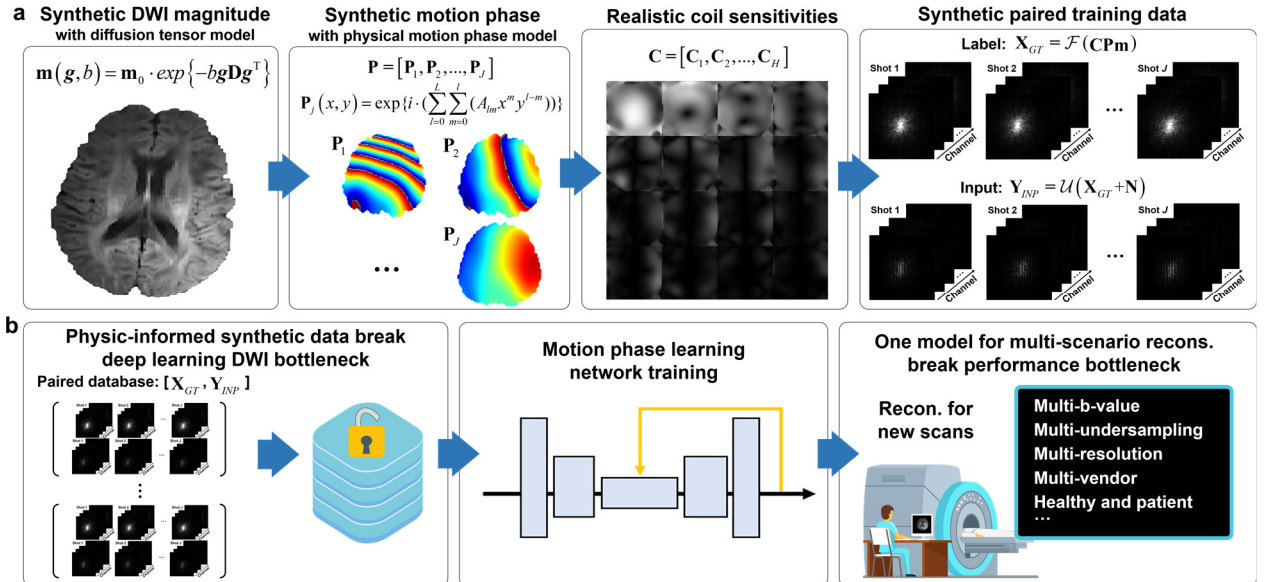


**Fig. 2 | Physics-informed deep diffusion MRI (PIDD) breaks the bottleneck of obtaining training data in deep learning reconstructions.** (a) A large amount of motion phases and DWI magnitudes are synthesized according to physical modeling (diffusion tensor model for DWI magnitude synthesis, and inter-shot motion-induced phase model for motion phase synthesis), which are combined with realistic sensitivity maps to generate training labels. Then, the paired training data are generated from training labels by adding Gaussian noise and undersampling, retrospectively. (b) Physics-informed data synthesis by PIDD breaks the bottleneck of obtaining training data in deep learning DWI reconstruction. PIDD, which is trained only once with the synthetic database (100,000 samples), has good performance and generalization on multi-scenario reconstructions, including multi-b-value (1000, 2000, 3000, 4000 s/mm<sup>2</sup>), multi-resolution (1.5×1.5, 1.2×1.2, 1.0×1.0 mm<sup>2</sup>), multi-undersampling (partial Fourier at rate of 0.7, 0.8), and multi-vendor (3.0T Philips Ingenia CX, 3.0T Philips Ingenia DNA, and 3.0T United Imaging uMR 890).

parameters ( $g$  and  $b$ ) are provided, the magnitude of diffusion signal  $\mathbf{m}$  can be synthesized according to Eq. (1).

The motion phase is generated according to a physically derived polynomial phase model<sup>24</sup> with increased orders:

$$\mathbf{P}(x, y) = \exp\{i \cdot \phi(x, y)\} = \exp\left\{i \cdot \left(\sum_{l=0}^L \sum_{m=0}^l (A_{lm} x^m y^{l-m})\right)\right\}, \quad (2)$$

where  $(x, y)$  is the image coordinate,  $L$  is the order of the polynomial model, and  $A_{lm}$  is the coefficients of  $x^m y^{l-m}$ . Once these parameters are set, a large amount of motion phases can be generated by Eq. (2).

The coil sensitivity map  $\mathbf{C}$  is estimated from realistic T2-weighted MRI data. Then, the synthesized magnitude, motion phase, and realistic coil sensitivity maps are combined to get multi-channel, multi-shot DWI data as the ground truth  $\mathbf{X}_{GT}$ :

$$\mathbf{X}_{GT} = \mathcal{F}(\mathbf{C}\mathbf{P}\mathbf{m}). \quad (3)$$

For the network design, the most critical part is learning motion phases, especially high-order motion phases. In our network (Supplementary Note 1), these phases are modeled as motion kernels in the k-space<sup>25</sup>, and we employ multiple learnable convolution kernels to learn these motion kernels. After trained with a large amount of synthetic training data, the PIDD network can gradually estimate motion phase accurately (Supplementary Note 1), leading to successful artifacts removal of magnitude images. PIDD network has significantly fast speed of training label synthesis (~0.72 hours per 1000 samples) and testing data reconstruction (~2 seconds per sample), which is 150 times faster than traditional optimization methods (~300 seconds per sample with PAIR, see Supplementary Note 2).

The PIDD trained with 100,000 synthetic data is compared with state-of-the-art (SOTA) optimization and DL methods on realistic four-shot iEPI DWI datasets. **DATASET I (Healthy volunteer DTI)**: acquired on a 3.0T scanner in Xiamen, China (Ingenia CX, Philips Healthcare). Seven healthy volunteers are included. Matrix size is  $180 \times 180$  ( $1.5 \times 1.5 \text{ mm}^2$ ), b-values are 0 and 1000 s/mm<sup>2</sup>, and diffusion direction is 12. **DATASET II (Healthy volunteer DWI)**: acquired on a 3.0T scanner in Shanghai, China (uMR 890, United Imaging Healthcare). One healthy volunteer is scanned. Matrix sizes are  $160 \times 160$  ( $1.5 \times 1.5 \text{ mm}^2$ ) and  $230 \times 224$  ( $1.0 \times 1.0 \text{ mm}^2$ ), and b-values are 0, 1000, 2000, 3000, and 4000 s/mm<sup>2</sup>. **DATASET III (Patient DTI)**: acquired on a 3.0T scanner in Zhengzhou, China (Ingenia DNA, Philips Healthcare). Nine patients are included. Matrix size is  $220 \times 180$  ( $1.0 \times 1.2 \text{ mm}^2$ ), b-values are 0 and 1000 s/mm<sup>2</sup>, diffusion directions are 12, and partial Fourier undersampling rate is 0.6. Other clinical protocols are also acquired as references. **DATASET IV (Patient DWI)**: acquired on a 3.0T scanner in Shanghai, China (Ingenia, Philips Healthcare).

Thirteen patients are included. Matrix size is  $228 \times 228$  ( $1.0 \times 1.0 \text{ mm}^2$ ), b-values are 0 and 1000 s/mm<sup>2</sup>, and partial Fourier undersampling is 0.7.

PIDD can be interpreted well in estimating motion phases, particularly on higher-order phases (Fig. 1 and Fig. 3). It also shows good clinical adaptability to patient DTI data (Fig. 4). As the optimization method assumes smooth motion phases<sup>29,30</sup>, neither PAIR nor the conventional DL method, which uses the PAIR-reconstruction as the label, can reconstruct images with high-order motion phases (2<sup>nd</sup> and 3<sup>rd</sup> columns in Fig. 1 and Fig. 3(e)). This limitation results in spurious image features (Fig. 1(j, k), Fig. 3 (i,j) and Fig. 4(m)) or signal loss (Fig. 3(b) and Fig. 4(c,d)). PIDD can handle high-order phases (Fig. 1(h) and Fig. 3(g) and Fig. 4(e)) and leads to much better reconstructed images (Fig. 1(l), Fig. 3(d)). Seven experienced doctors blindly score image quality (Fig. 4) to 3.8~3.9 points, which lies in good confidence (point range: 3~4) and approaches to excellence (point range: 4~5) for clinical diagnosis.

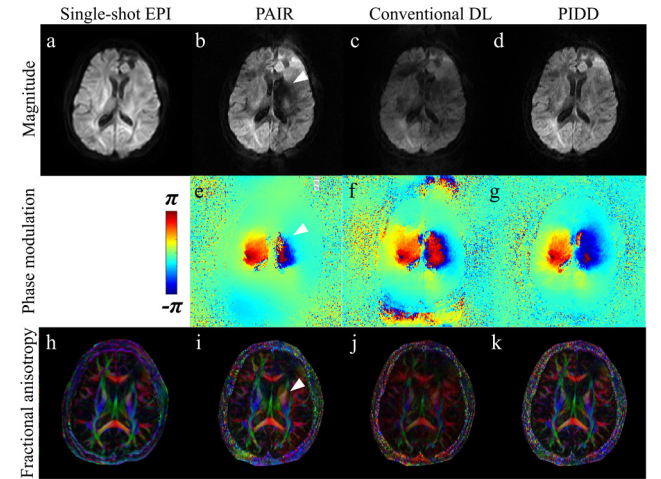


**Fig 3 | Comparison of conventional deep learning (DL) method and the proposed PIDD on *in vivo* patient DTI (DATASET III) that exhibits high-order motion phases.** The single-shot EPI DWI without inter-shot motion artifacts is employed as a reference. The fractional anisotropy images are calculated from 16 DWI images with different diffusion directions. Conventional DL is trained on DATASET I with 1296 *in vivo* samples, and the labels are generated by PAIR. PIDD is trained with 100,000 synthetic samples with 5-order motion phases. Signal loss and spurious features of PAIR are marked with white arrows.

PIDD also provides best motion artifacts removal (lowest ghost-to-signal ratio in Supplementary Note 2) and outstanding generalization for multi-scenario reconstructions (Fig. 5). Since conventional DL methods need optimization-based reconstruction as the training labels, the difference between the data used for the optimization method and the target imaging data leads to obvious signal loss in images (Fig. 5(h)-(m)). If the optimization method fails, artifacts will be presented in



conventional DL results (Fig. S2 (g, i)). PIDD overcomes these limitations very well and further generalized well to multi-scenarios (Figs. 5(o)-(u) and Supplementary Notes 2 and 5), including multi-resolution, multi-b-value, multi-undersampling rates, and multi-vendor scanners.

In conclusion, PIDD exploits the power of MRI physics for deep learning DWI, presents an easy, generalizable, and explainable way to obtain training data, and shows great potential for clinical diagnosis.

## RESULTS

### Adaptability to patient data

We first examine the adaptability of PIDD on patient DTI **DATASET III**, which is essential in clinical diagnosis. PAIR, MoDL, and PIDD reconstruct DTI data collected from 9 patients, and each patient's DTI has 18 slices and 16 diffusion directions (2592 samples in total). MoDL is trained with realistic data (six

cases from DATASET I, 108 slices  $\times$  12 directions = 1296 training samples), and the training labels is reconstructed by PAIR with optimized parameters. PIDD is trained once with 100,000 synthetic samples. Thus, both MoDL and PIDD have never seen any patient data.

MRI images of a 25-year-old female patient after surgery for brain diffuse astrocytoma are shown in Fig. 4. T2-weighted (Fig. 4(a)), contrast-enhanced T1-weighted (Fig. 4(f)) and fluid-attenuated inversion recovery (Fig. 4(k)) images are used for tumor diagnosis. The single-shot EPI DWI and the corresponding mean diffusivity (MD) and fractional anisotropy (FA) images are employed as references for evaluation (Fig. 4(b, g, l)) since they do not involve multi-shot imaging thus are free of motion artifacts.

The left frontal lobe lesion presents high signal on T2-weighted image (Fig. 4(a)), no obvious enhancement on

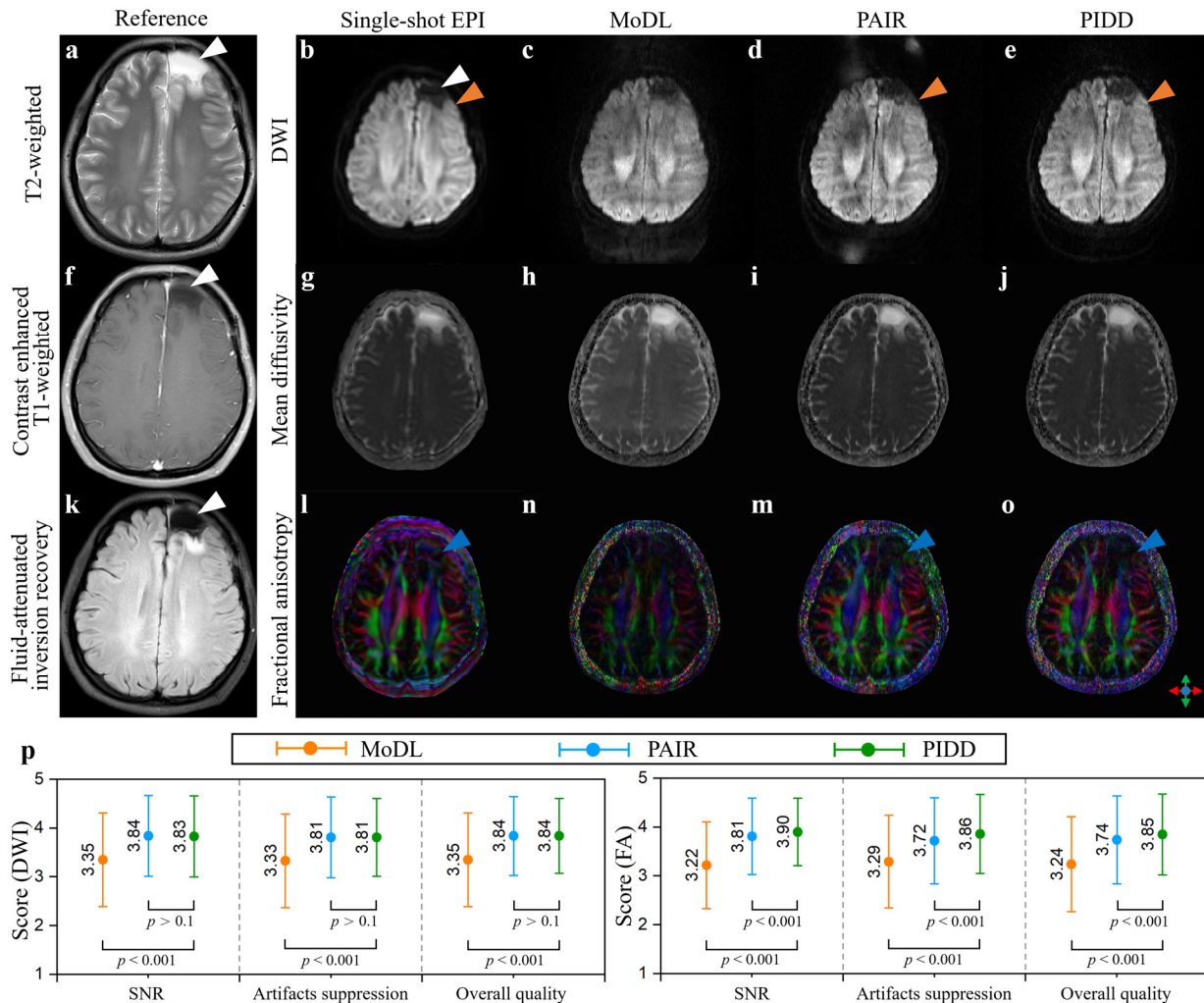


**Fig. 4 | Clinical study on DATASET III patient DTI.** (a)-(o) are the reconstructed patient DWI images by MoDL (1.4 seconds per image), PAIR (287.3 seconds per image), and PIDD (2 seconds per image). T2 weighted, contrast enhanced T1 weighted, fluid attenuated inversion recovery, and single-shot EPI DWI images without inter-shot motion artifacts are employed as references, and the region of interest are marked by white arrows. The incorrect structures are marked by yellow arrows. (p) are the score comparisons of the reader study on selected DWI images (43 slices contains tumors or diseased regions from nine patients). Note: The mean values and standard deviations are computed over all tested patients. Wilcoxon signed-rank test is used for scores analysis.  $p < 0.001$  indicates the difference between two compared methods is statistically significant, while  $p > 0.1$  indicates no significant difference.



contrast-enhanced T1-weighted image (Fig. 4(f)), and low signal on fluid-attenuated inversion recovery image (Fig. 4(k)) and single-shot DWI (Figs. 4(b)), indicating that the lesion area is the signal of postoperative fluid accumulation. Thus, there is no fibrous link in the lesion area, and FA should be no signal.

However, the MD and FA of MoDL differs greatly from references (Figs. 4(c, h, n)). PAIR introduces wrong structural features in the reconstructed images (yellow arrow in Fig. 4(d)) because the displayed region is larger than the reference regions in the structured image (Figs. 4(a, f, k)) or single-shot DWI image (Fig. 4(b)).

The proposed PIDD provides DWI images without noticeable motion artifacts and incorrect structures (Figs. 4(e, j, o)). PIDD also has the matched lesion region with reference DWI images (Fig. 4(b)). Moreover, the lesion area in FA of PIDD (blue arrow in Fig. 4(o)) shows weaker signal, which is more consistent with the real pathology than FA image of PAIR (blue arrow in Fig. 4(m)).

Four more patient DTI (Figs. S4-S7) from **DATASET III** and thirteen more patient DWI cases (Fig. S8) from **DATASET VI** are shown in Supplementary Notes 4, 5, and 6, which also confirm the advantage of PIDD on reconstructing better DWI, MD and FA images.

From a diagnostic perspective, a reader study (Fig. 4(p)) is conducted to evaluate PIDD on patient data. Seven readers (five radiologists with 5/8/13/20/30 years' experience and two neurosurgeons with 9/26 years' experience) are invited to independently score the image quality of reconstruction. Clinically used low-resolution single-shot DWI images, which

are free of inter-shot motion artifacts, are provided as references. Readers are blind to all patient information and reconstruction methods.

In total, 43 slices from 9 patients containing tumors or diseased regions are selected for evaluation, and each slice has 16 diffusion directions. For each slice, reconstructed DWI and generated FA are used for scoring. Three clinical criteria are employed for evaluation: signal-to-noise ratio (SNR), artifact suppression, and overall image quality. Each criterion's score is ranged from 0 to 5 with a precision of 0.1. The difference in scores between PIDD and the compared methods are analyzed with the Wilcoxon signed-rank test.

For FA estimated from 16 diffusion directions, PIDD has achieved scores in the range of 3.85~3.90, which show statistical advantages over PAIR and MoDL ( $p < 0.001$ ). For DWI images, scores of PAIR and PIDD are around 3.81, which are similar and show no statistical difference. From a diagnostic perspective, PIDD achieves scores that lie in the range of good (3.0~4.0) and are close to excellence (4.0~5.0), and are significantly superior to MoDL. The full report for all individual readers is in Supplementary Note 3.

Reader study demonstrates that PIDD can provide high-resolution DWIs of patients that have good and even approach excellent diagnostic values.

#### Generalizable reconstruction for multiple scenarios

The generalization ability of PIDD is tested on **DATASET II** (Fig. 5), which contains DWI data with multi-b-value and multi-resolution. To emulate the mismatch, MoDL is trained on **DATASET I**. Reconstruction parameters of PAIR are optimized

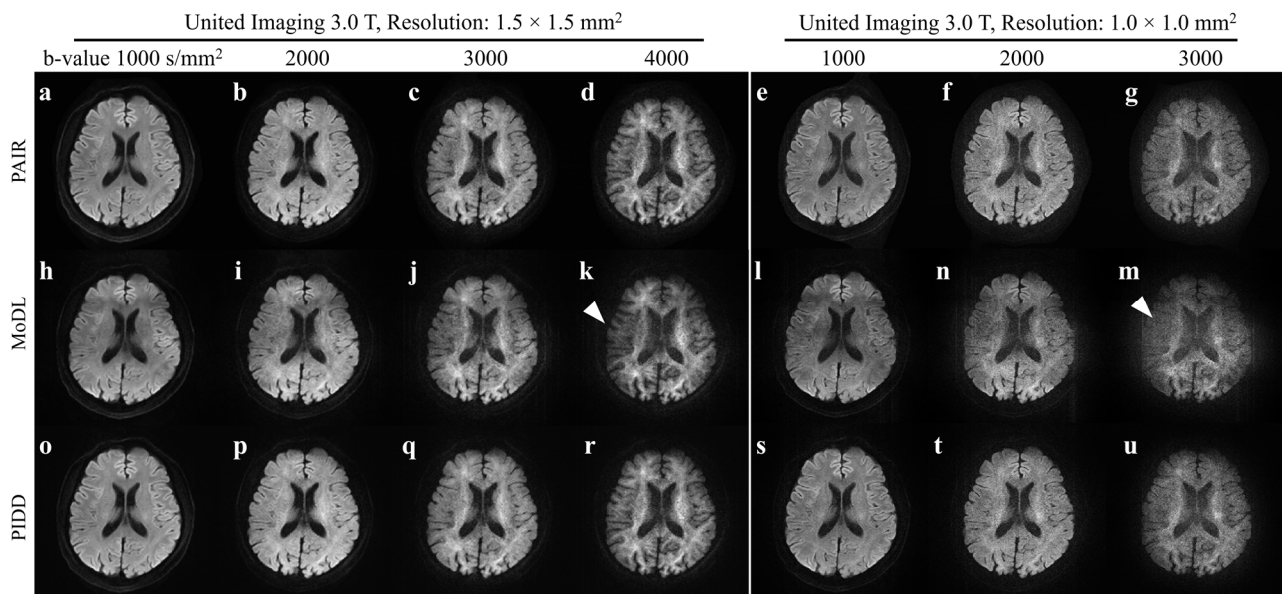


**Fig. 5 | Generalization study on DATASET II of healthy volunteer DWI.** (a)-(u) are trace DWI images calculated by three diffusion direction DWI images. The incorrect contrast induced by motion artifacts and noise residual are marked by white arrows. Note: Reconstruction parameters of PAIR are optimized on each image to get the best removal of motion artifacts. MoDL is trained on **DATASET I** with 1296 *in vivo* real samples. PIDD is trained with 100,000 synthetic samples.

on each image to get the best motion artifact removal. PAIR results are used to evaluate the performance of two DL methods, MoDL and PIDD, under multiple-scenario reconstructions.

For MoDL (Figs. 5(h)-(m)), the large mismatch between the training and testing data results in noticeable artifacts. Its trace DWI images combined from three diffusion directions have severe mistakes (arrows in Figs. 5(k, m)), including structural errors, incorrect contrast, and significant noise corruption with ultra-high b-values (b-value=4000 s/mm<sup>2</sup>).

For PIDD (Figs. 5(o)-(u)), it shows great generalization on multi-b-value (1000, 2000, 3000, and 4000 s/mm<sup>2</sup>), multi-resolution (1.5 × 1.5 mm<sup>2</sup> and 1.0 × 1.0 mm<sup>2</sup>), multi-vendor (Philips data in Fig. 4 and United Imaging data in Fig. 5), and multi-undersampling-rate (partial Fourier undersampling with sampling rates of 0.7, and 0.8 in Supplementary Note 2)

This good generalization of PIDD is due to the flexible training data synthesis. First, multi-b-value DWI images can be easily synthesized by the diffusion tensor model. Second, the Gaussian noise added to k-space has a wide range to cover diverse noise levels in realistic multi-b-value data. The data synthesis process is detailed in the section of Methods.

These results demonstrate that PIDD achieves a better generalization over the compared DL method under multiple DWI reconstruction scenarios.

## Discussion and conclusion

### Explainable motion phase learning

PIDD has the advantage of high-order phase preservation over conventional methods, leading to better artifact removal on both synthetic (Fig. 1) and *in vivo* image reconstructions (Figs. 3, 4, 5). This advantage is not only attributed to data synthesis, but also the neural network design.

PIDD network (Supplementary Notes 1) is proposed to learn the motion kernels from synthetic data with high-order motion phases with multiple convolution kernels in the training stage. In the reconstruction stage, the estimated motion kernels perform missing data k-space interpolations between shots. The visualized motion kernels further show that PIDD well preserves high-order components of motion phase modulations and provides better magnitude images than PAIR (Supplementary Notes 5 and 6).

### Limitations of PIDD.

PIDD, like other DL methods, has the following restrictions: (a) PIDD cannot obtain satisfactory reconstructions for ultra-high shot numbers, such as 8 shots<sup>9,27</sup>. Although it is not clinically necessary to pursue ultra-high shot numbers due to its prolonged acquisition time, some modifications on PIDD may help improve its performance on 8-shot DWI data. For example,

PIDD may increase its iteration numbers of low-rank constraints to handle a higher number of shots<sup>30</sup>. In this scenario, it is more appropriate to think of PIDD as a provider of a good initial solution for the optimization algorithms. (b) Only brain reconstructions were tested in this work. The data synthesis approach may fail for other organs that have more complex motions. For example, the liver DWI is expected to have a higher order motion phase induced by elastic motions<sup>38</sup>, which is hard to be synthesized currently.

## Conclusion

In summary, we proposed PIDD, a novel and promising physics-informed deep learning framework, for exploiting the power of diffusion MRI physics to break the bottleneck of obtaining high-quality training data in multi-shot DWI image reconstruction. PIDD presents an easy and cost-effective way to synthesize large-scale paired DWI databases for network training. It outperforms state-of-the-art optimization and deep learning methods both in healthy and patient studies, providing more accurate diffusion quantitative maps for patients with seven experienced doctors' verifications.

## Methods

### Physics-informed DWI data synthesis

For ms-iEPI DWI, each image shot is assumed to share the same magnitude  $\mathbf{m}$ , but has a different phase<sup>22</sup>. The  $j$ -th shot of image  $\mathbf{I}_j$  can be represented as:

$$\mathbf{I}_j = \mathbf{P}_j \mathbf{m} = e^{-i\phi} e^{-i\phi_j} \mathbf{m}, \quad (4)$$

where the background phase  $e^{-i\phi}$  and motion-induced extra phase  $e^{-i\phi_j}$  are combined to get the shot phase  $\mathbf{P}_j$ . Since both the background and motion phases are commonly assumed to be smooth and vary slowly<sup>22</sup>,  $\mathbf{P}_j$  is approximately smooth.

As introduced above, physics-informed DWI data generation involves synthesizing the motion phase (the background phase is included in the motion phase to simplify the synthesis), magnitude images, coil sensitivity maps, and the addition of Gaussian noise.

### Physics-informed motion phase synthesis.

The major sources of macroscopic motion in brain DWI are involuntary head motion and pulsatile brain motion<sup>24,39</sup>. The former can be modeled as rigid motion, such as shift and rotation, introducing low-order motion phases. The latter is generally considered brain parenchymal motions and cerebrospinal fluid pulsations<sup>39,40</sup>, resulting in high-order motion phases. We use a high-order polynomial motion phase model to synthesize the motion phase (Eq. 2).

Experimentally, this phase model is designed to fit the realistic motion phase well. We obtain realistic motion phases by the conventional optimization method PAIR<sup>30</sup>. Then, a phase

unwrapping method<sup>41</sup> is employed to unroll the motion phases. We test the performance of phase models of different orders on fitting the real phase (Fig. 6). A larger  $L$  shows a better fitting of complex shot phases. In our scheme,  $L = 5$  is selected to balance computational complexity and accuracy. For  $l = 0, 1, 2, 3, 4, 5$ ,  $A^{lm}$  are randomly distributed in  $[-\pi, \pi)$ ,  $[-\pi, \pi)$ ,  $[-\pi, \pi)$ ,  $[-\pi/2, \pi/2)$ ,  $[-\pi/2, \pi/2)$ ,  $[-\pi/2, \pi/2)$ .

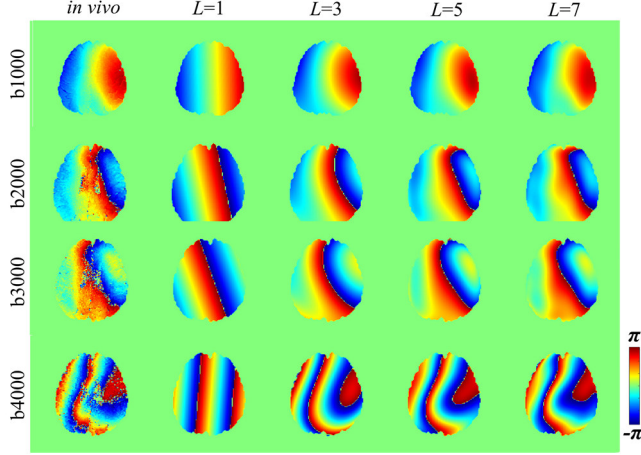


**Fig 6 | Representatively synthesized motion phases.** The *in vivo* motion phases of 4-shot DWI with different b-values (1000, 2000, 3000 s/mm<sup>2</sup>) and corresponding synthetic motion phases with different polynomial order ( $L = 1, 3, 5, 7$ ) are shown.

#### Physics-informed DWI magnitude synthesis.

The DTI model in Eq. (1) is employed for magnitude synthesis. We acquire a set of DWI images from a 3.0T Philips Ingenia CX scanner to get a high-quality diffusion tensor. The image set contains two non-diffusion images and 64 DWI images (b-value=1000 s/mm<sup>2</sup>) with uniformly distributed diffusion directions. Then, the diffusion tensor is calculated with the Python package DIPY<sup>42</sup>.

When the high-quality diffusion tensor and non-diffusion image are known in Eq. (1), the magnitude of diffusion signal  $m(g, b)$  with given diffusion direction and b-value can be synthesized. The given  $g$  are  $[0,0,1]$ ,  $[0,1,0]$ ,  $[1,0,0]$ , and  $b$  are 1000, 2000, 3000, and 4000 s/mm<sup>2</sup>.

300 realistic coil sensitivity maps are estimated by ESPIRiT<sup>43</sup> from 16-channel T<sub>2</sub> weighted MRI data (16×16 k-space center are cropped) from the Fast MRI database<sup>44</sup>.

The synthesized motion phase, magnitude, and realistic coil sensitivity maps are combined to get multi-channel, multi-shot DWI data. Then, these data are transformed to k-space and added Gaussian noise to decrease the signal-to-noise-ratio (SNR) to the range of 10-50 dB. Fig. 7 shows the synthesized magnitude images with different b-values after adding noise.

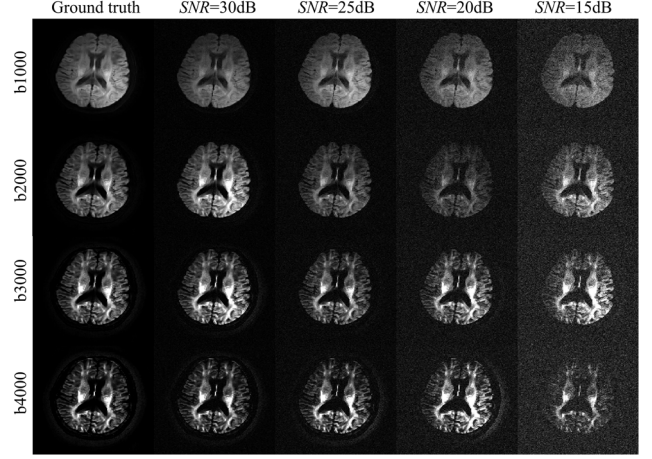


**Fig 7 | Representatively synthesized DWI magnitude images with the added noise.** The diffusion direction is  $[0,0,1]$ , and b-values are 1000, 2000, 3000, and 4000 s/mm<sup>2</sup>. The Gaussian noise is added in the k-space to decrease the SNR to 30, 25, 20, and 15 dB, respectively.

#### Methods for comparisons

One state-of-the DL method (MODL<sup>9</sup>) and optimization method (PAIR<sup>30</sup>) are used for comparison. MoDL is a generalization of the MUSSELS<sup>28</sup>, which exploits cross-shot annihilating filter relations deduced from smooth phase modulations, and the interpolates missing data in k-space from multi-shot data by a structured low-rank matrix completion formulation<sup>29</sup>, with similar performance but much faster reconstruction speed<sup>9</sup>. PAIR employs an iteratively joint estimation model with the paired priors of phase and magnitude to regularize the reconstruction<sup>30</sup>. In this work, the MoDL is trained on DATASET I with 1296 samples, and training labels are reconstructed by PAIR. Besides, MUSSELS<sup>28</sup> is also compared in Supplementary Notes 5 and 6.

#### Evaluation criteria

One objective and three subjective metrics are adopted to assess reconstruction. Ghost-to-signal ratio (GSR) is utilized to evaluate the motion artifact suppression quantitatively, and a lower GSR means better artifact removal. Three clinical-concerned subjective metrics are adopted in the reader study, including image SNR, artifact suppression, and overall image quality. The single-shot DWI and DTI images are provided as references. Each criterion's score ranges from 0 to 5 with precision of 0.1 (i.e., 0~1: Non-diagnostic; 1~2: Poor; 2~3: Adequate; 3~4: Good; 4~5: Excellent). The reader study is performed on our cloud computing evaluation platform, CloudBrain-ReconAI<sup>45,46</sup>, which is free to access at <https://csrc.xmu.edu.cn/CloudBrain.html>.

#### Data preprocessing and postprocessing

Four DWI databases are collected in this work, and all experiments are Institutional Review Board-approved and



volunteer-informed. Before reconstructions, the echo-planar imaging ghost is carefully corrected by a widely employed reference-free method<sup>47</sup>. Few ghost residuals, however, may still exist in some images. All DWI data are coil compressed<sup>48</sup> to no more than 16 channels to reduce computational complexity.

For reconstructions, coil sensitivity maps are estimated by ESPIRiT<sup>43</sup> with non-diffusion data. DTI metrics such as FA, MD, and diffusion tensors are calculated using the Python package DIPY<sup>42</sup>.

## Data availability

The PIDD training data and model will be shared respectively at

<https://github.com/qianchne/PIDD>

<https://csrc.xmu.edu.cn/CloudBrain.html>

Other collected DWI databases are available from the corresponding author upon a reasonable request.

## References

- Zhu, B., Liu, J. Z., Cauley, S. F., Rosen, B. R. & Rosen, M. S. Image reconstruction by domain-transform manifold learning. *Nature*, 555, 487-492 (2018).
- Knoll, F. et al. Deep-learning methods for parallel magnetic resonance imaging reconstruction: A survey of the current approaches, trends, and issues. *IEEE Signal Processing Magazine*, 37, 128-140, (2020).
- Yang, Y., Sun, J., Li, H. & Xu, Z. ADMM-CSNet: A deep learning approach for image compressive sensing. *IEEE Transactions on Pattern Analysis and Machine Intelligence*, 42, 521-538, (2020).
- Perlman, O. et al. Quantitative imaging of apoptosis following oncolytic virotherapy by magnetic resonance fingerprinting aided by deep learning. *Nature Biomedical Engineering*, 6, 648-657, (2022).
- Vishnevskiy, V., Walheim, J. & Kozerke, S. Deep variational network for rapid 4D flow MRI reconstruction. *Nature Machine Intelligence*, 2, 228-235, (2020).
- Wang, S. et al. in 2016 IEEE 13th international symposium on biomedical imaging (ISBI). 514-517 (2016).
- Wang, Z. et al. One-dimensional deep low-rank and sparse network for accelerated MRI. *IEEE Transactions on Medical Imaging*, 42, 79-90, (2022).
- Liu, S. et al. Learning MRI artefact removal with unpaired data. *Nature Machine Intelligence*, 3, 60-67, (2021).
- Aggarwal, H. K., Mani, M. P. & Jacob, M. MoDL-MUSSELS: model-based deep learning for multi-shot sensitivity-encoded diffusion MRI. *IEEE Transactions on Medical Imaging*, 39, 1268-1277 (2019).
- Yakimovich, A., Beaugnon, A., Huang, Y. & Ozkirimli, E. Labels in a haystack: Approaches beyond supervised learning in biomedical applications. *Patterns*, 2, 12, (2021).
- Bammer, R. et al. Diffusion-weighted imaging with navigated interleaved echo-planar imaging and a conventional gradient system. *Radiology*, 211, 799-806, (1999).
- Wang, F. et al. In vivo human whole-brain connectome diffusion MRI dataset at 760  $\mu\text{m}$  isotropic resolution. *Scientific Data*, 8, 122, (2021).
- Zhang, H. et al. Deep learning based multiplexed sensitivity-encoding (DL-MUSE) for high-resolution multi-shot DWI. *NeuroImage*, 244, 118632, (2021).
- Qian, C. et al. in *20th IEEE International Symposium on Biomedical Imaging (ISBI)*, doi: 10.1109/ISBI53787.2023.10230538. (2023)
- Jones, D. K. Diffusion MRI. (Oxford University Press, 2010).
- Gao, A. et al. Whole-tumor histogram analysis of multiple diffusion metrics for glioma genotyping. *Radiology*, 302, 652-661, (2022).
- McKay, J. A. et al. A comparison of methods for high-spatial-resolution diffusion-weighted imaging in breast MRI. *Radiology*, 297, 304-312, (2020).
- Fiebach, J. et al. CT and diffusion-weighted MR imaging in randomized order: Diffusion-weighted imaging results in higher accuracy and lower interrater variability in the diagnosis of hyperacute ischemic stroke. *Stroke*, 33, 2206-2210, (2002).
- Mukherjee, P., Berman, J., Chung, S., Hess, C. & Henry, R. Diffusion tensor MR imaging and fiber tractography: theoretic underpinnings. *American Journal of Neuroradiology*, 29, 632-641 (2008).
- An, H., Ma, X., Pan, Z., Guo, H. & Lee, E. Y. P. Qualitative and quantitative comparison of image quality between single-shot echo-planar and interleaved multi-shot echo-planar diffusion-weighted imaging in female pelvis. *European Radiology*, 30, 1876-1884 (2020).
- Skare, S. et al. Clinical multi-shot DW-EPI through parallel imaging with considerations of susceptibility, motion, and noise. *Magnetic Resonance in Medicine*, 57, 881-890 (2010).
- Chen, N.-k., Guidon, A., Chang, H.-C. & Song, A. W. A robust multi-shot scan strategy for high-resolution diffusion weighted MRI enabled by multiplexed sensitivity-encoding (MUSE). *Neuroimage*, 72, 41-47 (2013).
- Liu, C. et al. A resource for the detailed 3D mapping of white matter pathways in the marmoset brain. *Nature Neuroscience*, 23, 271-280, (2020).
- Anderson, A. W. & Gore, J. C. Analysis and correction of motion artifacts in diffusion weighted imaging. *Magnetic Resonance in Medicine*, 32, 379-387, (1994).
- Ma, X., Zhang, Z., Dai, E. & Guo, H. Improved multi-shot diffusion imaging using GRAPPA with a compact kernel. *NeuroImage*, 138, 88-99, (2016).
- Herbst, M. et al. Prospective motion correction with continuous gradient updates in diffusion weighted imaging. *Magnetic Resonance in Medicine*, 67, 326-338, (2012).
- Hu, Y. et al. RUN-UP: Accelerated multishot diffusion-weighted MRI reconstruction using an unrolled network with U-Net as priors. *Magnetic Resonance in Medicine*, 85, 709-720, (2020).
- Mani, M., Aggarwal, H. K., Magnotta, V. & Jacob, M. Improved MUSSELS reconstruction for high-resolution multi-shot diffusion weighted imaging. *Magnetic Resonance in Medicine*, 83, 2253-2263, (2020).
- Mani, M., Jacob, M., Kelley, D. & Magnotta, V. Multi-shot sensitivity-encoded diffusion data recovery using structured low-rank matrix completion (MUSSELS). *Magnetic Resonance in Medicine*, 78, 494-507 (2017).
- Qian, C. et al. A paired phase and magnitude reconstruction for advanced diffusion-weighted imaging. *IEEE Transactions on Biomedical Engineering*, doi:10.1109/TBME.2023.3288031 (2023).
- Karniadakis, G. E. et al. Physics-informed machine learning.

*Nature Reviews Physics*, 3, 422-440, (2021).

32 Yang, Q., Wang, Z., Guo, K., Cai, C. & Qu, X. Physics-driven synthetic data learning for biomedical magnetic resonance: The imaging physics-based data synthesis paradigm for artificial intelligence. *IEEE Signal Processing Magazine*, 40, 129-140 (2023).

33 Kaandorp, M. P. T. et al. Improved unsupervised physics-informed deep learning for intravoxel incoherent motion modeling and evaluation in pancreatic cancer patients. *Magnetic Resonance in Medicine*, 86, 2250-2265, (2021).

34 Chen, R. J., Lu, M. Y., Chen, T. Y., Williamson, D. F. & Mahmood, F. Synthetic data in machine learning for medicine and healthcare. *Nature Biomedical Engineering*, 5, 493-497 (2021).

35 Tian, Q. et al. DeepDTI: High-fidelity six-direction diffusion tensor imaging using deep learning. *NeuroImage*, 219, 117017 (2020).

36 Barbieri, S., Gurney-Champion, O. J., Klaassen, R. & Thoeny, H. C. Deep learning how to fit an intravoxel incoherent motion model to diffusion-weighted MRI. *Magnetic Resonance in Medicine*, 83, 312-321, (2020).

37 Le Bihan, D. et al. Diffusion tensor imaging: concepts and applications. *Journal of Magnetic Resonance Imaging*, 13, 534-546 (2001).

38 Geng, R. et al. Motion-robust, blood-suppressed, reduced-distortion diffusion MRI of the liver. *Magnetic Resonance in Medicine*, 89, 908-921, (2023).

39 Bammer, R. Basic principles of diffusion-weighted imaging. *European Journal of Radiology*, 45, 169-184 (2003).

40 Greitz, D. et al. Pulsatile brain movement and associated hydrodynamics studied by magnetic resonance phase imaging: the Monro-Kellie doctrine revisited. *Neuroradiology*, 34, 370-380 (1992).

41 Karsa, A. & Shmueli, K. SEGUE: A speedy region-growing algorithm for unwrapping estimated phase. *IEEE Transactions on Medical Imaging*, 38, 1347-1357, (2019).

42 Garyfallidis, E. et al. Dipy, a library for the analysis of diffusion MRI data. *Frontiers in Neuroinformatics*, 8, 8 (2014).

43 Uecker, M. et al. ESPIRiT—an eigenvalue approach to autocalibrating parallel MRI: where SENSE meets GRAPPA. *Magnetic Resonance in Medicine*, 71, 990-1001 (2014).

44 Zbontar, J. et al. fastMRI: An open dataset and benchmarks for accelerated MRI. arXiv preprint arXiv:1811.08839 (2018).

45 Zhou, Y. et al. CloudBrain-ReconAI: An online platform for MRI

reconstruction and image quality evaluation. arXiv preprint arXiv:2212.01878 (2022).

46 Zhou, Y. et al. in *2021 43rd Annual International Conference of the IEEE Engineering in Medicine & Biology Society (EMBC)*. 3289-3292.

47 McKay, J. A. et al. Nyquist ghost correction of breast diffusion weighted imaging using referenceless methods. *Magnetic resonance in medicine*, 81, 2624-2631 (2019).

48 Zhang, T., Pauly, J. M., Vasanawala, S. S. & Lustig, M. Coil compression for accelerated imaging with Cartesian sampling. *Magnetic Resonance in Medicine*, 69, 571-582, (2013).

## Acknowledgements

The authors thank Dr. Mathews Jacob for sharing their codes online. This work was supported in part by the National Natural Science Foundation of China under grants 62122064, 62331021, 61971361 and 62371410, Natural Science Foundation of Fujian Province of China under grants 2023J02005 and 2021J011184, President Fund of Xiamen University under grant 20720220063, and Nanqiang Outstanding Talent Program of Xiamen University.

## Author contributions

X. Qu and C. Qian conceived the idea and designed the experiments, X. Qu supervised the project, C. Qian, Y. Gao, and M. Han implemented the method, processed databases, and produced results, C. Qian, Y. Gao and D. Ruan drew the figures for the manuscript and supplementary. Y. Shen, C. Wang, J. Wang, Z. Wu, B. Jiang, R. Tao, J. Zhou, and M. Wang helped to acquire in vivo data. Y. Zhou, Y. Guo, T. Gong, G. Fei, L. Zhu, T. Kang, J. Lin, and C. Yang conducted the reader study. The manuscript was drafted by C. Qian and improved by Z. Wang, M. Lin, Y. Shen, Y. Wu, D. Guo, and X. Qu. X. Qu and D. Guo acquired research funds and provided all the needed resources.

## Competing interests

B. Jiang, and R. Tao are employees of United Imaging Healthcare, China; Z. Wu, and J. Wang are employees of Philips Healthcare, China.

## Supplementary Information

### Note 1. PIDD network architecture and implementation

The PIDD network has  $K$  learnable iteration and output blocks (Fig. S1). Each iteration block contains the data consistency and motion kernel learning modules.

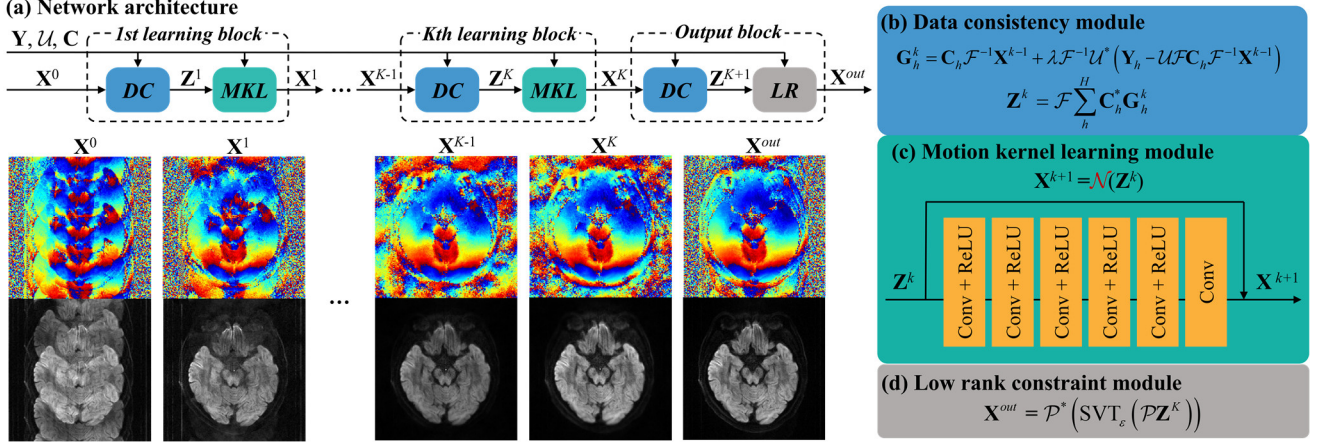


**Figure S1 | The architecture of the PIDD network.** (a) The iteration blocks include (b) a data consistency (DC) module, (c) a motion kernel learning (MKL) module, and (d) a low-rank constraint (LR) module. Note: Conv is the convolutional layer, and ReLU is a widely employed activation function.

### Motion kernel interpolation model

We first deduce that the motion phase in the image domain can be modeled as the motion kernel in the k-space. Then, we introduce a k-space interpolation model with a motion kernel for ms-iEPI DWI reconstruction.

The  $i^{\text{th}}$  shot image  $I_i$  and  $j^{\text{th}}$  shot image have the relationship:

$$I_i = P_i m = P_i \frac{P_j^\dagger P_j}{P_j^\dagger P_j} m = P_i \frac{P_j^\dagger}{P_j^\dagger P_j} P_j m = P_i \frac{P_j^\dagger}{P_j^\dagger P_j} I_j = \hat{P}_{ij} I_j, \quad (S1)$$

where  $P_i \frac{P_j^\dagger}{P_j^\dagger P_j} = \hat{P}_{ij}$  is the motion phase modulation, and the superscript  $\dagger$  is the complex conjugate.

Performing the Fourier transform on the two side of Eq. (S1), and we get a convolution form in k-space:

$$X_i = \mathcal{G}_{ij} X_j, \quad (S2)$$

where  $X_i$  and  $X_j$  are the k-space of  $i^{\text{th}}$  and  $j^{\text{th}}$  shot images and  $\mathcal{G}_{ij}$  is a convolution kernel determined by  $\hat{P}_{ij}$ .

Furthermore, we build a structured matrix  $P$  consisting of motion phase modulations  $\hat{P}_{ij}$ , which has the relationships between all shot images:

$$PI = \frac{1}{J-1} \begin{bmatrix} 0 & \hat{P}_{12} & \hat{P}_{13} & \dots & \hat{P}_{1J} \\ \hat{P}_{21} & 0 & \hat{P}_{23} & \dots & \hat{P}_{2J} \\ \hat{P}_{31} & \hat{P}_{32} & 0 & \dots & \hat{P}_{3J} \\ \vdots & \vdots & \vdots & 0 & \vdots \\ \hat{P}_{J1} & \hat{P}_{J2} & \hat{P}_{J3} & \dots & 0 \end{bmatrix} \begin{bmatrix} I_1 \\ \vdots \\ I_j \\ \vdots \\ I_J \end{bmatrix} = \begin{bmatrix} I_1 \\ \vdots \\ I_j \\ \vdots \\ I_J \end{bmatrix}. \quad (S3)$$



Perform the Fourier transform on Eq. (S3) by substituting multiplication in the image space with the convolution operator in Eq. (S2), and we get:

$$\mathbf{GX} = \frac{1}{J-1} \begin{bmatrix} 0 & \mathcal{G}_{12} & \mathcal{G}_{13} & \cdots & \mathcal{G}_{1J} \\ \mathcal{G}_{21} & 0 & \mathcal{G}_{23} & \cdots & \mathcal{G}_{2J} \\ \mathcal{G}_{31} & \mathcal{G}_{32} & 0 & \cdots & \mathcal{G}_{3J} \\ \vdots & \vdots & \vdots & 0 & \vdots \\ \mathcal{G}_{J1} & \mathcal{G}_{J2} & \mathcal{G}_{J3} & \cdots & 0 \end{bmatrix} \begin{bmatrix} \mathbf{X}_1 \\ \vdots \\ \mathbf{X}_j \\ \vdots \\ \mathbf{X}_J \end{bmatrix} = \begin{bmatrix} \mathbf{X}_1 \\ \vdots \\ \mathbf{X}_j \\ \vdots \\ \mathbf{X}_J \end{bmatrix} = \mathbf{X}. \quad (\text{S4})$$

Then, we proposed a k-space interpolation model with motion kernel:

$$\min_{\mathbf{X}} \sum_{h=1}^H \left\| \mathbf{Y}_h - \mathcal{U} \mathcal{F} \mathbf{C}_h \mathcal{F}^{-1} \mathbf{X} \right\|_{\text{F}}^2 + \frac{\lambda}{2} \left\| \mathbf{GX} - \mathbf{X} \right\|_{\text{F}}^2, \quad (\text{S5})$$

where  $\mathbf{Y}_h$  is the sampled  $h^{\text{th}}$  channel k-space data,  $\mathcal{U}$  is the undersampling operator,  $\mathcal{F}$  and  $\mathcal{F}^{-1}$  are the Fourier transform and inverse Fourier transform operator,  $\mathbf{C}_h$  is the  $h^{\text{th}}$  channel coil sensitivity map,  $\lambda$  is the regularization parameter, and subscript F represents the Frobenius norm.

We take the POCS (Projection Onto Convex Sets) algorithm to solve this model, and the  $k^{\text{th}}$  iteration contains:

$$\begin{cases} \mathbf{G}_h^k = \mathbf{C}_h \mathcal{F}^{-1} \mathbf{X}^{k-1} + \lambda \mathcal{F}^{-1} \mathcal{U}^* (\mathbf{Y}_h - \mathcal{U} \mathcal{F} \mathbf{C}_h \mathcal{F}^{-1} \mathbf{X}^{k-1}) \\ \mathbf{Z}^k = \mathcal{F} \left( \sum_h^H \mathbf{C}_h^* \mathbf{G}_h^k \right) \\ \mathbf{X}^{k+1} = \mathcal{G}(\mathbf{Z}^k) \end{cases} \quad (\text{S6})$$

To make it work in real scenarios where  $\mathcal{G}$  is unknown, we replace  $\mathcal{G}$  with a learnable network  $\mathcal{N}$  in the following motion kernel learning model:

$$\min_{\mathbf{X}} \sum_{h=1}^H \left\| \mathbf{Y}_h - \mathcal{U} \mathcal{F} \mathbf{C}_h \mathcal{F}^{-1} \mathbf{X} \right\|_{\text{F}}^2 + \frac{\lambda}{2} \left\| \mathcal{N}(\mathbf{X}) - \mathbf{X} \right\|_{\text{F}}^2, \quad (\text{S7})$$

where  $\mathcal{N}$  is a convolution neural network for motion kernel learning. We also take the POCS (Projection Onto Convex Sets) algorithm to solve this model and unrolled the solving process into two modules: data consistency and motion kernel learning.

#### Data consistency module

The projection operator for data consistency is used to project the initial image onto a convex set. The convex set contains all images that have the same value as the acquired data at sampled k-space positions (Fig. S1(b)):

$$\mathbf{G}_h^k = \mathbf{C}_h \mathcal{F}^{-1} \mathbf{X}^{k-1} + \lambda \mathcal{F}^{-1} \mathcal{U}^* (\mathbf{Y}_h - \mathcal{U} \mathcal{F} \mathbf{C}_h \mathcal{F}^{-1} \mathbf{X}^{k-1}), \quad (\text{S8})$$

$$\mathbf{Z}^k = \mathcal{F} \left( \sum_h^H \mathbf{C}_h^* \mathbf{G}_h^k \right), \quad (\text{S9})$$

where the superscript  $*$  is the adjoint operation, and the regularization parameter  $\lambda$  is set to 1. This module has no learnable parameters.

#### Motion kernel learning module

The  $\mathcal{G}$  derived from the motion phase provides the interpolation kernels between the shot images in the k-space. Here, we employ a convolution network  $\mathcal{N}$  as the projection operator to learn the motion kernels:

$$\mathbf{X}^{k+1} = \mathcal{N}(\mathbf{Z}^k), \quad (\text{S10})$$

where  $k$  donates the index of the iteration block, and the total number of blocks is  $K = 10$ .

The  $\mathcal{N}$  has six layers, and each is composed of 48 convolution kernels of size 3. The parameters can be updated in the supervised training stage. In the reconstruction stage, these convolution kernels in  $\mathcal{N}$  play the role of motion kernels  $\mathcal{G}$  to interpolate among the shot images in the k-space.

---

### Low-rank constraint module

The proposed network cannot recover unsampled data in widely employed partial Fourier undersampling, since the motion kernel interpolation fails to do extrapolation. Thus, we use an output module to extrapolate by exploiting the low-rankness property. The low-rankness-based data recovery is commonly adopted in traditional methods<sup>1,2</sup>.

$$\mathbf{X}^{out} = \mathcal{P}^* \left( \text{SVT}_{\varepsilon} \left( \mathcal{P} \mathbf{Z}^{K+1} \right) \right), \quad (\text{S11})$$

where  $\text{SVT}_{\varepsilon}$  is the singular value thresholding operator<sup>3</sup>, and the first  $\varepsilon$  singular values are saved.  $\mathcal{P}$  is the operator for the structured low-rank matrix construction<sup>2,4</sup>, and  $\mathcal{P}^*$  is the adjoint operator of  $\mathcal{P}$ .

### Loss function and implementation details

The loss function is:

$$\mathcal{L} = \frac{1}{KT} \sum_{t=1}^T \sum_{k=1}^K \left\| \mathbf{X}^{k,t} - \mathbf{X}_{GT}^t \right\|_F^2, \quad (\text{S12})$$

where  $T$  is the number of training samples,  $K$  is the output of the  $k^{\text{th}}$  block with  $t^{\text{th}}$  training samples as input,  $\mathbf{X}_{GT}^t$  is the  $t^{\text{th}}$  label, and  $\mathbf{X}^{k,t}$  is the output of  $k^{\text{th}}$  block.

In the training stage, the weights of the reconstruction network are Xavier initialized and trained with  $T = 100,000$  synthetic training samples by Adam optimizer. Its initial learning rate is 0.001, with an exponential decay of 0.99. The batch size is 1, block number  $K$  is 10, and the training takes about 120 hours on a Nvidia Tesla T4 GPU (16 GB memory) with TensorFlow 1.15.0. After training, the PIDD model is employed for *in vivo* data reconstruction. If the *in vivo* data have partial Fourier undersampling, a low-rank constraint module is performed ten times.

## Note 2. Comparisons with state-of-the-art (SOTA) methods

The proposed PIDD is compared with two optimization methods, including PAIR<sup>2</sup> and MUSSELS<sup>5</sup>, and one DL method MoDL<sup>6</sup> on 144 testing samples from DATASET I (Fig. S2). MoDL is trained with realistic data (six cases from DATASET I, 108 slices  $\times$  12 directions = 1296 training samples), and the training labels is reconstructed by PAIR with optimized parameters. PIDD is trained once with 100,000 synthetic samples.

Serious motion artifacts (Fig. S2(a) and (f)) are observed if a trivial inverse Fourier transform (IFT) is applied, resulting in high ghost-to-signal ratio (GSR)<sup>7</sup> and many outliers (Fig. S2(k)). This observation implies that motion-induced phase and artifacts have a significant variance among different data. Thus, robust reconstruction of 144 testing samples is challenging.

SOTA methods are sensitive to samples. Algorithm parameters of PAIR and MUSSELS are optimized to successfully remove most artifacts for the first sample (Figs. S2(b) and (c)) but may degrade image quality for another sample that has a different slice and diffusion direction (Figs. S2(g) and (h)). This sensitivity also limits the performance of MoDL since its training labels are PAIR reconstructions. Thus, MoDL always has worse GSR than PAIR (Fig. S2(k)). Even though, MoDL is still very valuable as its reconstruction time is greatly reduced than PAIR (Fig. S2(l)).

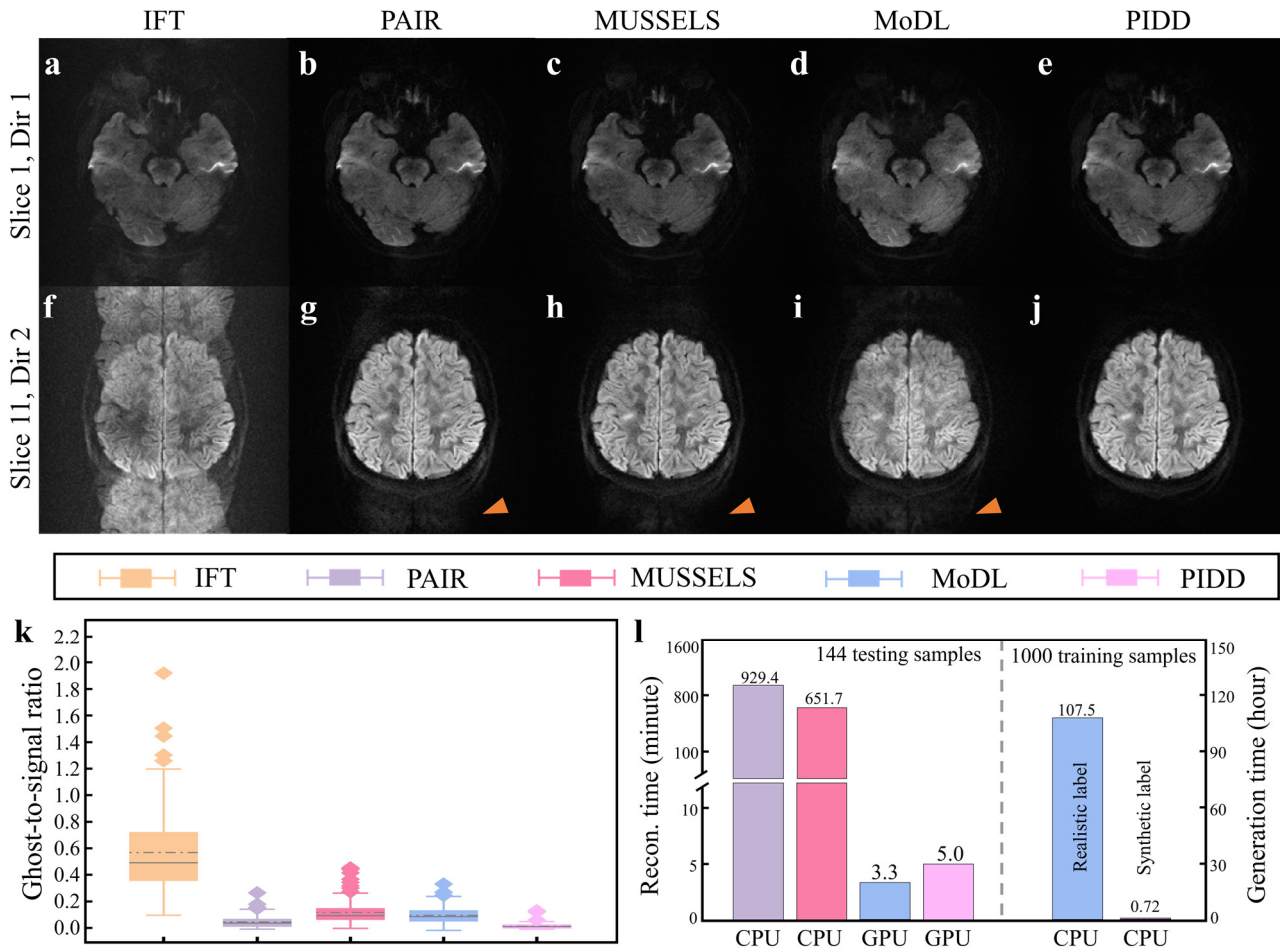


**Figure S2 | Comparison study on the DATASET I of healthy volunteer DTI.** (a)-(j) are the reconstructed DWI images by the methods for comparisons and PIDD. Motion artifact residuals are marked by yellow arrows (the second row). (k) is the ghost-to-noise ratio (GSR) calculated on 144 DWI images. (l) are the comparisons of reconstruction time of PAIR, MUSSELS, MoDL, and PIDD, respectively, and label generation time of MoDL, and PAIR. Note: IFT is the inverse Fourier transform. The hardware platform employed for all algorithms is a server with Intel Xeon Silver 4210 CPUs (256 GB RAM), and Nvidia Tesla T4 GPU (16 GB memory).



PIDD synthesizes the training data much faster (more than 100 times in Fig. S2(l)) and the reconstruction is more robust than all compared methods. PIDD suppresses the motion artifacts very well on these samples (Figs. S2(e) and (j)) and achieves the lowest GSR (Fig. S2(k)).

Partial Fourier undersampling is commonly adopted in scanners for fast imaging. PIDD removes artifacts more efficiently and preserves image sharpness better than other SOTA methods under partial Fourier undersampling (Fig. S3), further indicating its robustness.

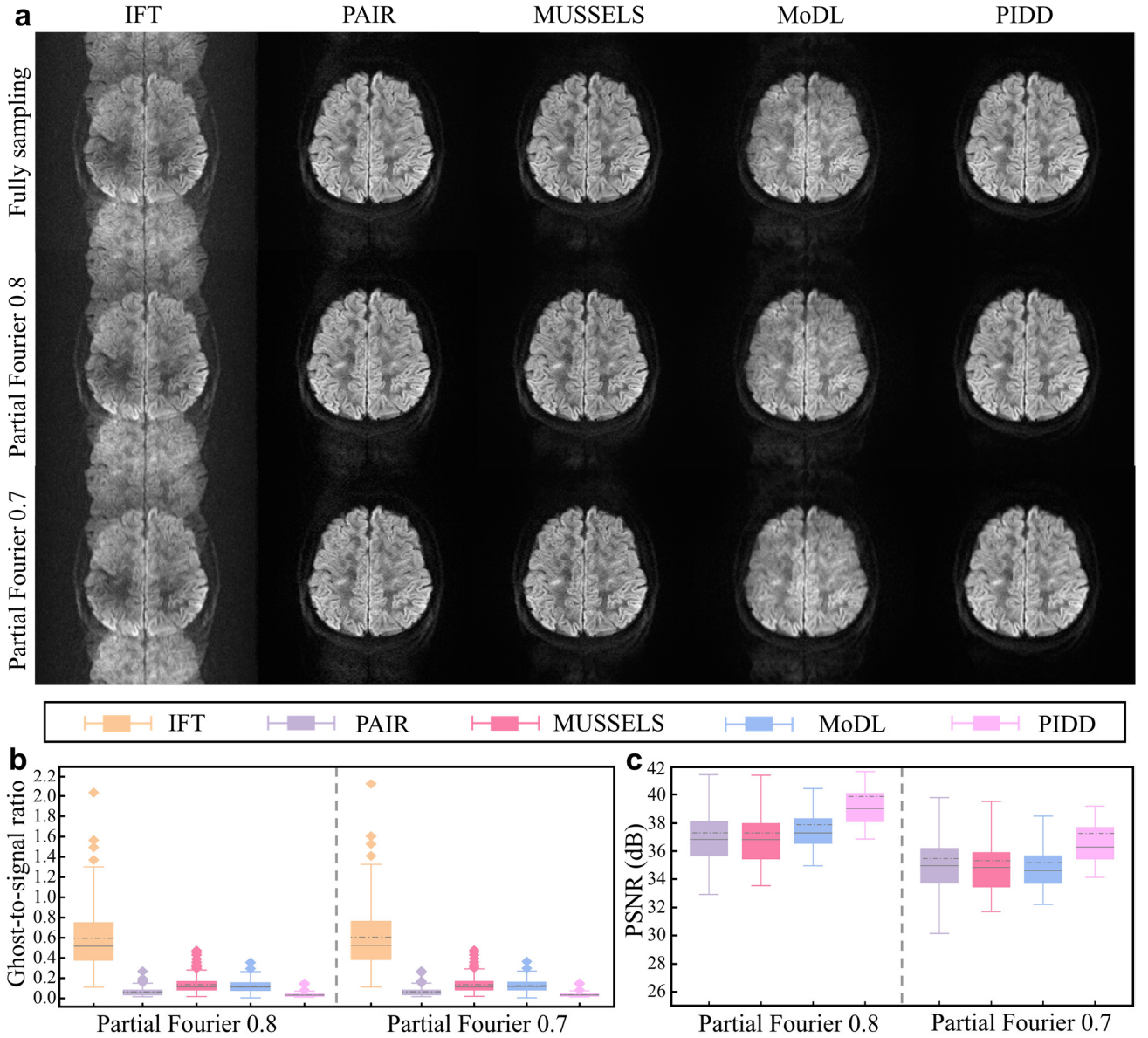


**Figure S3 | Comparison study on DATASET I under partial Fourier undersampling. (a)** are the reconstructed DWI images by comparison methods and PIDD. **(b)** are the ghost-to-noise ratios calculated on 144 DWI images. **(c)** are the PSNR of partial Fourier undersampling, and the ground truth for PSNR calculation is the corresponding fully sampled images (without partial Fourier undersampling). Note: IFT is the inverse Fourier transform.

**Note 3. Individual scores of 7 neuro readers (5 radiologists with 5/8/13/20/30 years' experience and 2 neurosurgeons with 9/26 years' experience)**

**Table 1 | Scores (mean  $\pm$  standard deviation) of DWI images**

Reader	Criterion	MoDL	PAIR	PIDD
#1	Overall image quality	3.60 $\pm$ 0.15	<b>4.01<math>\pm</math>0.28</b>	4.00 $\pm$ 0.19
	SNR	3.64 $\pm$ 0.19	<b>4.04<math>\pm</math>0.27</b>	4.01 $\pm$ 0.19
	Artifact suppression	3.56 $\pm$ 0.25	<b>3.93<math>\pm</math>0.29</b>	3.92 $\pm$ 0.21
#2	Overall image quality	2.26 $\pm$ 0.98	3.41 $\pm$ 1.09	<b>3.50<math>\pm</math>0.83</b>
	SNR	2.29 $\pm$ 0.97	3.52 $\pm$ 1.09	<b>3.65<math>\pm</math>0.94</b>
	Artifact suppression	2.24 $\pm$ 1.02	3.41 $\pm$ 1.22	<b>3.62<math>\pm</math>0.85</b>
#3	Overall image quality	4.58 $\pm$ 0.07	4.77 $\pm$ 0.11	<b>4.79<math>\pm</math>0.09</b>
	SNR	4.57 $\pm$ 0.08	<b>4.74<math>\pm</math>0.09</b>	<b>4.74<math>\pm</math>0.09</b>
	Artifact suppression	4.55 $\pm$ 0.08	4.74 $\pm$ 0.11	<b>4.76<math>\pm</math>0.09</b>
#4	Overall image quality	2.18 $\pm$ 0.65	<b>2.93<math>\pm</math>0.62</b>	2.84 $\pm$ 0.53
	SNR	2.20 $\pm$ 0.63	<b>2.93<math>\pm</math>0.62</b>	2.83 $\pm$ 0.51
	Artifact suppression	2.17 $\pm$ 0.60	<b>2.92<math>\pm</math>0.66</b>	2.70 $\pm$ 0.66
#5	Overall image quality	3.23 $\pm$ 0.31	<b>3.38<math>\pm</math>0.31</b>	3.34 $\pm$ 0.31
	SNR	3.17 $\pm$ 0.31	<b>3.29<math>\pm</math>0.59</b>	3.17 $\pm$ 0.76
	Artifact suppression	3.20 $\pm$ 0.31	<b>3.38<math>\pm</math>0.30</b>	3.31 $\pm$ 0.31
#6	Overall image quality	3.83 $\pm$ 0.25	4.28 $\pm$ 0.21	<b>4.30<math>\pm</math>0.21</b>
	SNR	3.80 $\pm$ 0.22	4.22 $\pm$ 0.24	<b>4.26<math>\pm</math>0.20</b>
	Artifact suppression	3.80 $\pm$ 0.2	4.23 $\pm$ 0.22	<b>4.29<math>\pm</math>0.22</b>
#7	Overall image quality	3.77 $\pm$ 0.62	4.11 $\pm$ 0.67	<b>4.11<math>\pm</math>0.65</b>
	SNR	3.78 $\pm$ 0.63	<b>4.15<math>\pm</math>0.67</b>	4.13 $\pm$ 0.66
	Artifact suppression	3.77 $\pm$ 0.63	4.07 $\pm$ 0.67	<b>4.07<math>\pm</math>0.65</b>
Total	Overall image quality	3.35 $\pm$ 0.96	3.84 $\pm$ 0.81	<b>3.84<math>\pm</math>0.77</b>
	SNR	3.35 $\pm$ 0.95	<b>3.84<math>\pm</math>0.83</b>	3.83 $\pm$ 0.83
	Artifact suppression	3.33 $\pm$ 0.96	3.81 $\pm$ 0.83	<b>3.81<math>\pm</math>0.80</b>

Note: Best performance is marked with bold letters.

**Table 2 | Scores (mean  $\pm$  standard deviation) of fractional anisotropy (FA) images.**

Reader	Criterion	MoDL	PAIR	PIDD
#1	Overall image quality	3.47 $\pm$ 0.17	3.97 $\pm$ 0.31	<b>4.02<math>\pm</math>0.26</b>
	SNR	3.25 $\pm$ 0.21	3.96 $\pm$ 0.32	<b>4.00<math>\pm</math>0.28</b>
	Artifact suppression	3.63 $\pm$ 0.24	3.95 $\pm$ 0.34	<b>4.03<math>\pm</math>0.33</b>
#2	Overall image quality	1.78 $\pm$ 0.93	2.71 $\pm$ 1.21	<b>3.19<math>\pm</math>1.22</b>
	SNR	2.02 $\pm$ 0.80	3.22 $\pm$ 0.83	<b>3.61<math>\pm</math>0.64</b>
	Artifact suppression	1.98 $\pm$ 0.76	2.87 $\pm$ 0.87	<b>3.40<math>\pm</math>0.82</b>
#3	Overall image quality	4.58 $\pm$ 0.06	4.76 $\pm$ 0.08	<b>4.82<math>\pm</math>0.08</b>
	SNR	4.54 $\pm$ 0.07	4.74 $\pm$ 0.07	<b>4.78<math>\pm</math>0.07</b>
	Artifact suppression	4.60 $\pm$ 0.07	4.76 $\pm$ 0.10	<b>4.81<math>\pm</math>0.08</b>
#4	Overall image quality	2.36 $\pm$ 0.36	<b>2.92<math>\pm</math>0.36</b>	2.90 $\pm$ 0.29
	SNR	2.35 $\pm$ 0.36	<b>2.95<math>\pm</math>0.39</b>	2.90 $\pm$ 0.28
	Artifact suppression	2.36 $\pm$ 0.36	<b>2.94<math>\pm</math>0.40</b>	2.90 $\pm$ 0.30
#5	Overall image quality	2.97 $\pm$ 0.28	3.19 $\pm$ 0.32	<b>3.34<math>\pm</math>0.27</b>
	SNR	2.92 $\pm$ 0.30	3.09 $\pm$ 0.37	<b>3.33<math>\pm</math>0.29</b>
	Artifact suppression	2.83 $\pm$ 0.59	2.94 $\pm$ 0.76	<b>3.12<math>\pm</math>0.74</b>
#6	Overall image quality	3.67 $\pm$ 0.22	4.34 $\pm$ 0.30	<b>4.33<math>\pm</math>0.30</b>
	SNR	3.66 $\pm$ 0.21	<b>4.35<math>\pm</math>0.27</b>	4.35 $\pm$ 0.30
	Artifact suppression	3.67 $\pm$ 0.21	4.33 $\pm$ 0.28	<b>4.35<math>\pm</math>0.33</b>
#7	Overall image quality	3.77 $\pm$ 0.62	<b>4.11<math>\pm</math>0.65</b>	4.11 $\pm$ 0.67
	SNR	3.78 $\pm$ 0.63	4.13 $\pm$ 0.66	<b>4.15<math>\pm</math>0.67</b>
	Artifact suppression	3.77 $\pm$ 0.63	<b>4.07<math>\pm</math>0.65</b>	4.07 $\pm$ 0.67
Total	Overall image quality	3.24 $\pm$ 0.97	3.74 $\pm$ 0.90	<b>3.85<math>\pm</math>0.83</b>
	SNR	3.22 $\pm$ 0.89	3.81 $\pm$ 0.78	<b>3.90<math>\pm</math>0.69</b>
	Artifact suppression	3.29 $\pm$ 0.95	3.72 $\pm$ 0.88	<b>3.86<math>\pm</math>0.81</b>

Note: Best performance is marked with bold letters.



**Note 4. Representative patient images in the reader study**

We display four more patient cases from DATASET III reconstructed by PIDD and comparison methods (Fig. S4-S7), which have been employed in the reader study.

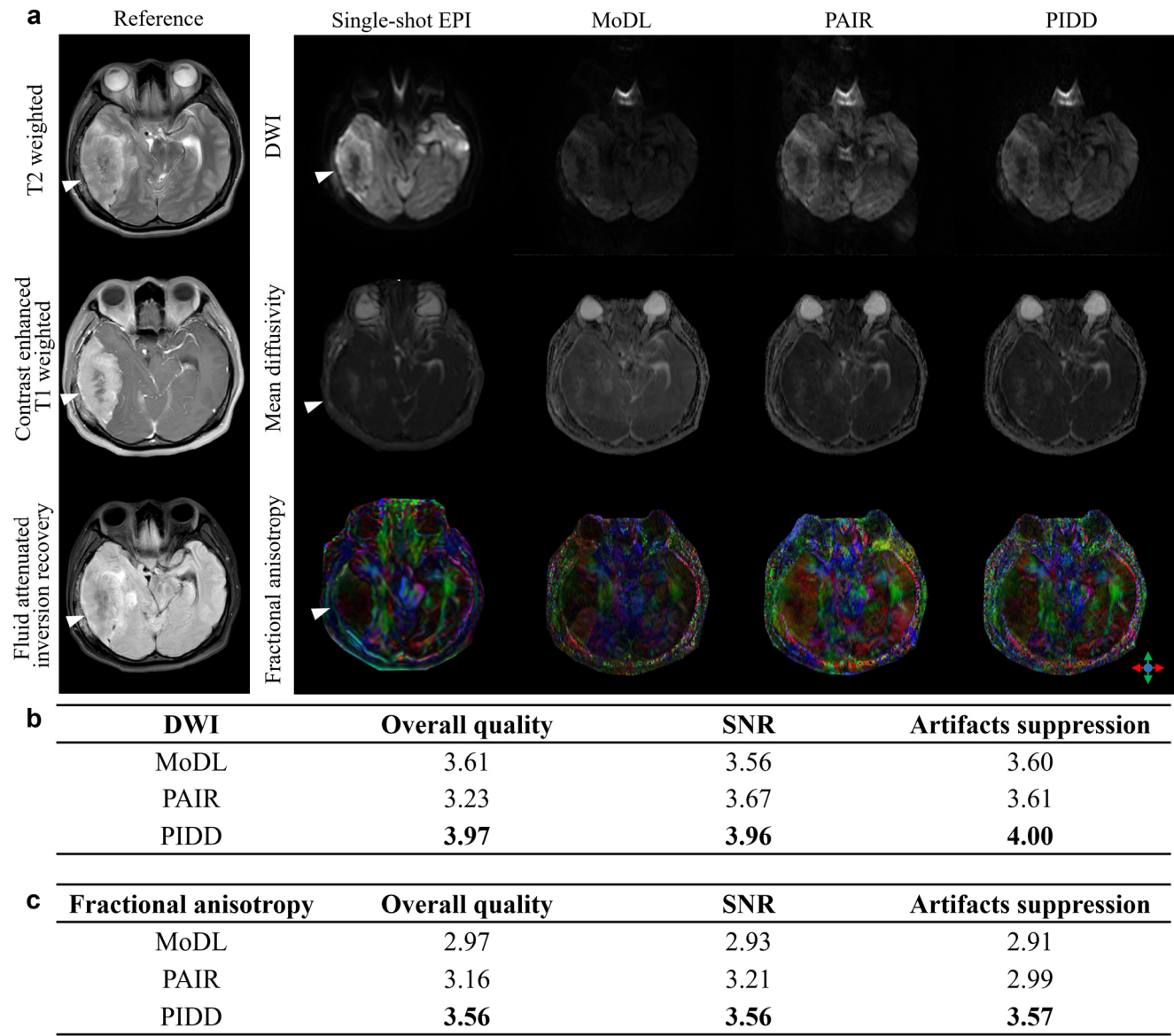


**Figure S4 | A patient (female, 34-year-old) with confirmed intracranial space-occupying lesions:** There is a space-occupying lesion in the right temporo-occipital region; An irregular mass-like slightly longer T1 signal shadow can be seen in the right temporo-occipital lobe; T2 and FLAIR show high and low mixed signals; Strip-like long T1 and long T2 signals can be seen in the inner edge; DWI shows high and low mixed signals. (a) are the reconstructed patient DWI, mean diffusivity, and fractional anisotropy images by MoDL, PAIR, and PIDD. T2 weighted, contrast enhanced T1 weighted, fluid attenuated inversion recovery, and single-shot EPI DWI images without inter-shot motion artifacts are employed as references. (b) and (c) are the score comparisons of the reader study on the selected DWI and fractional anisotropy images, respectively. Each score is an average of the scores given by 7 neuro readers (5 radiologists with 5/8/13/20/30 years' experience and 2 neurosurgeons with 9/26 years' experience). The lesions are marked with white arrows.

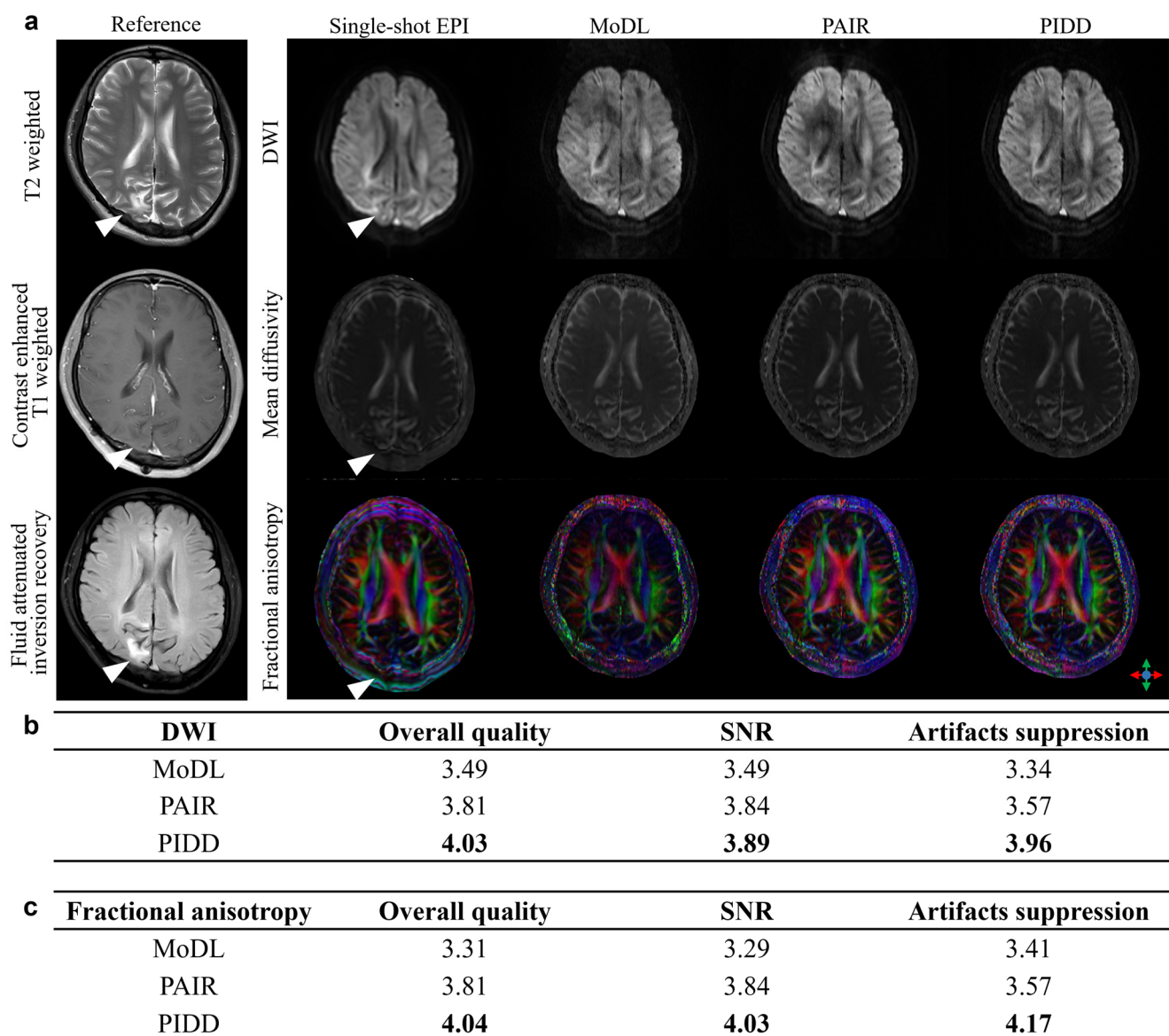


**Figure S5 | A patient (female, 39-year-old) with confirmed meningioma. The MR images are acquired after resection of the bilateral frontal-parietal area meningiomas adjacent to the sagittal sinuss: An irregular patchy space-occupying lesion is detected in the right occipital lobe. The lesion is low signal on T1WI, high signal on T2WI and FLAIR, slightly high signal on DWI, and no obvious enhancement on contrast-enhanced T1WI. The lesion is thought to be a possible recurrent meningioma. (a) are the reconstructed patient DWI, mean diffusivity, and fractional anisotropy images by MoDL, PAIR, and PIDD. T2 weighted, contrast enhanced T1 weighted, fluid attenuated inversion recovery, and single-shot EPI DWI images without inter-shot motion artifacts are employed as references. (b) and (c) are the score comparisons of the reader study on the selected DWI and fractional anisotropy images, respectively. Each score is an average of the scores given by 7 neuro readers (5 radiologists with 5/8/13/20/30 years' experience and 2 neurosurgeons with 9/26 years' experience). The lesions are marked with white arrows.**

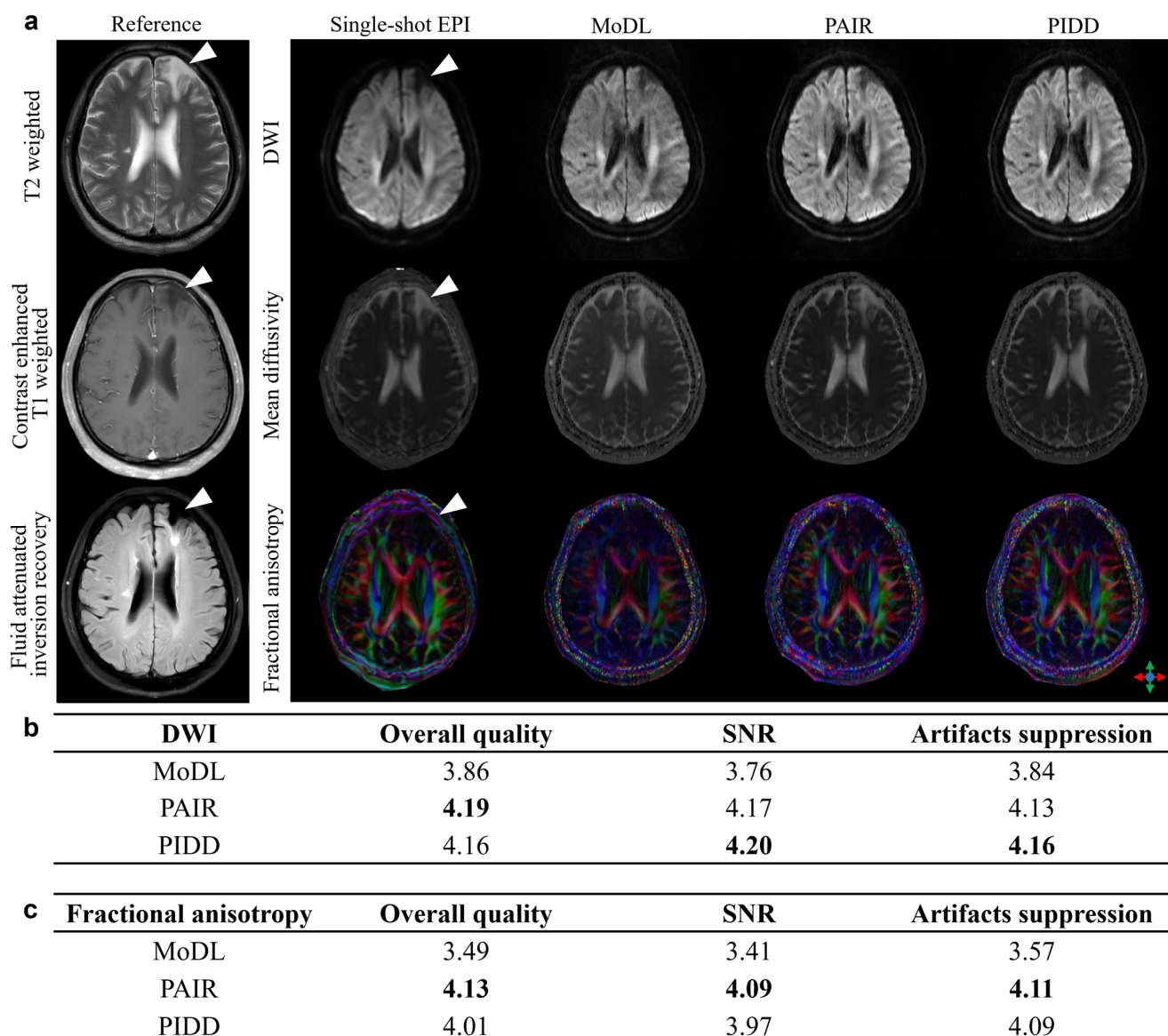


**Figure S6 | A patient (male, 61-year-old) with confirmed left lung adenocarcinoma: An irregular sheet-like lesion with well-defined borders was detected in the left frontal lobe with long T1 and long T2 and low signals on FLAIR and DWI. There was no significant enhancement on contrast-enhanced T1WI. The diagnosis was considered to be an encephalomalacia foci in the right frontal lobe.** (a) are the reconstructed patissant DWI, mean diffusivity, and fractional anisotropy images by MoDL, PAIR, and PIDD. T2 weighted, contrast enhanced T1 weighted, fluid attenuated inversion recovery, and single-shot EPI DWI images without inter-shot motion artifacts are employed as references. (b) and (c) are the score comparisons of the reader study on the selected DWI and fractional anisotropy images, respectively. Each score is an average of the scores given by 7 neuro readers (5 radiologists with 5/8/13/20/30 years' experience and 2 neurosurgeons with 9/26 years' experience). The lesions are marked with white arrows.

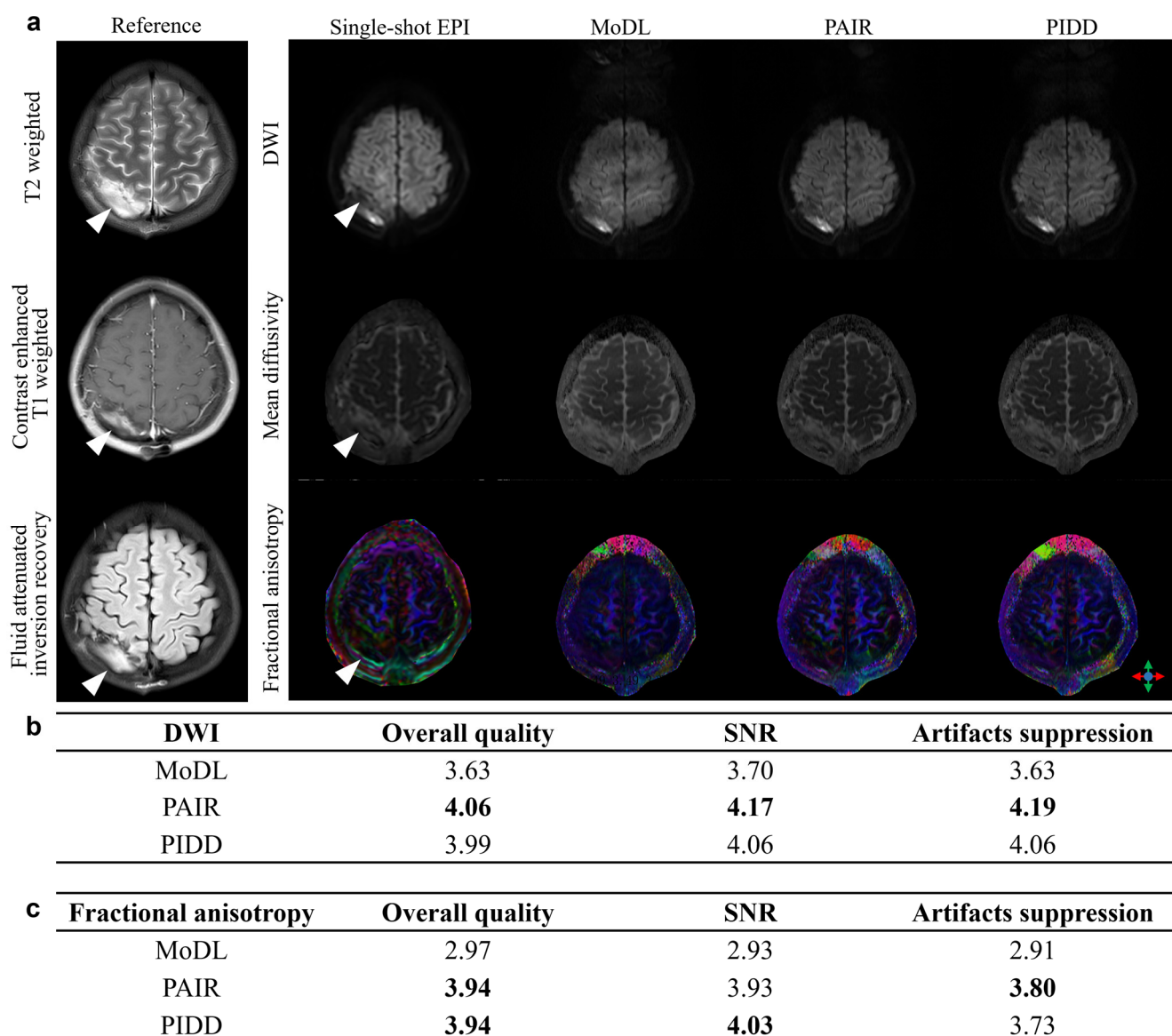


**Figure S7 | A patient (female, 13-year-old) with confirmed dysembryoplastic neuroepithelial tumor. The MR images are acquired after resection of the right parietal lobe lesion: An irregular sheet-like lesion is detected in the right parietal lobe with low signal on T1WI, high signal on T2 and FLAIR, inhomogeneous high signal on DWI, and significant enhancement on contrast-enhanced T1WI, which is clinically suspected to be a tumor recurrence. (a) are the reconstructed patient DWI, mean diffusivity, and fractional anisotropy images by MoDL, PAIR, and PIDD. T2 weighted, contrast enhanced T1 weighted, fluid attenuated inversion recovery, and single-shot EPI DWI images without inter-shot motion artifacts are employed as references. (b) and (c) are the score comparisons of the reader study on the selected DWI and fractional anisotropy images, respectively. Each score is an average of the scores given by 7 neuro readers (5 radiologists with 5/8/13/20/30 years' experience and 2 neurosurgeons with 9/26 years' experience). The lesions are marked with white arrows.**



### Note 5. Visualized phase modulation on DATASET IV (Patient DWI)

We reconstruct the DATASET IV with PAIR and the proposed PIDD, which includes 13 patients (13 patients  $\times$  15 slices  $\times$  3 diffusion directions = 585 images). PAIR uses a set of optimized and fixed parameters to reconstruct all images, while PIDD is trained on the synthetic data.

From the perspective of motion phase and motion kernel estimation, we analyze the reconstruction results in the yellow and green boxes (Fig. S8).

In Fig. S8, we visualize the motion kernels estimated by PIDD in the form of the motion phase modulations  $\mathbf{P}$ :

$$\mathbf{P} = \frac{1}{3} \begin{bmatrix} 0 & \hat{\mathbf{P}}_{12} & \hat{\mathbf{P}}_{13} & \hat{\mathbf{P}}_{14} \\ \hat{\mathbf{P}}_{21} & 0 & \hat{\mathbf{P}}_{23} & \hat{\mathbf{P}}_{24} \\ \hat{\mathbf{P}}_{31} & \hat{\mathbf{P}}_{32} & 0 & \hat{\mathbf{P}}_{34} \\ \hat{\mathbf{P}}_{41} & \hat{\mathbf{P}}_{42} & \hat{\mathbf{P}}_{43} & 0 \end{bmatrix}. \quad (\text{S14})$$

When the motion phase modulations are relatively low-order (green box in Fig. S8), both PAIR and PIDD can provide artifact-free magnitude images and share similar smooth motion phase modulations.

When the motion phase modulations become high-order (yellow box in the right part of Fig. S8), PAIR fails to remove artifacts, and the recovered motion phase modulations have unreasonable local smoothness. This over-smoothness is caused by the phase smooth constraints, which are widely employed as a prior in low-rank structured matrix completion methods<sup>1,2</sup>. However, PIDD preserves the high-order components of motion phase modulations well, providing a higher-quality magnitude image than PAIR.

The comparison demonstrates that the PIDD network can estimate the motion kernels corresponding to high-order motion phase modulations. Thus, PIDD surpasses conventional methods that are based on smooth phase assumption, achieving significant performance improvements.

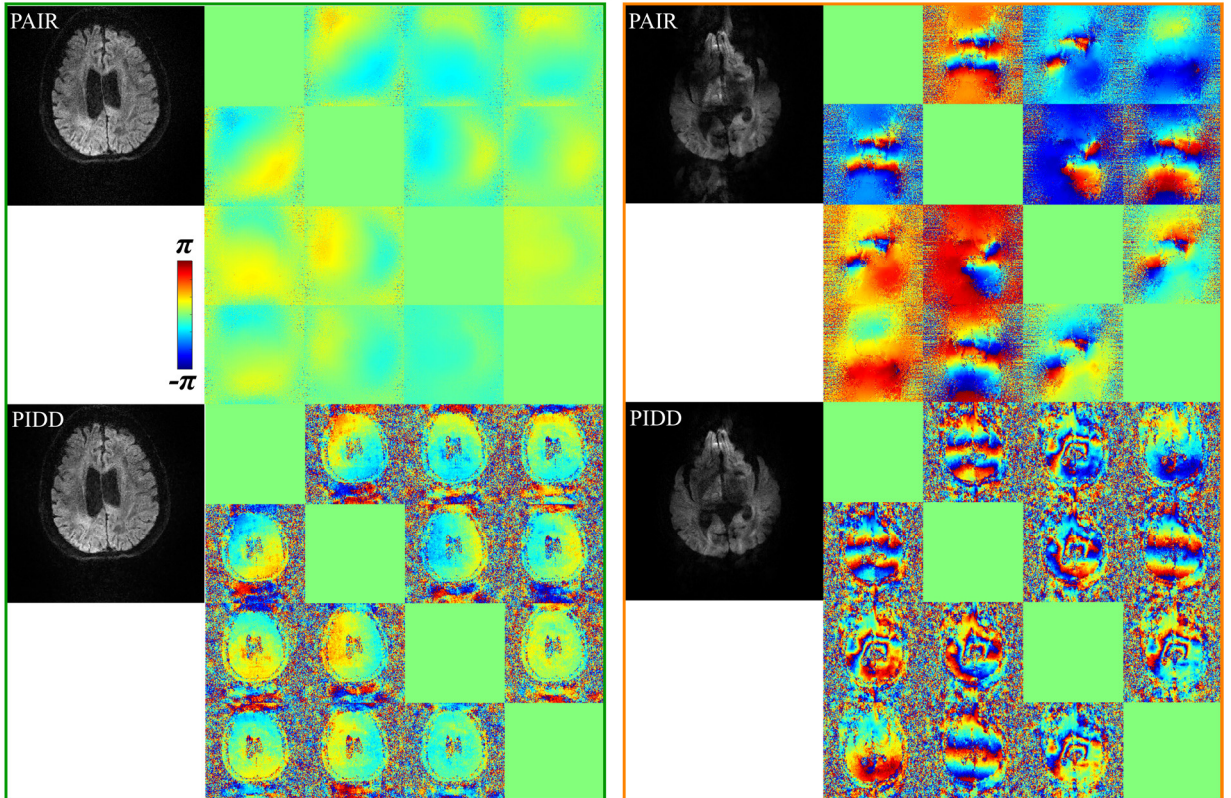


**Figure S8 | Visualization of low-order and high-order motion phase modulations.** DWI data from **DATASET IV** are reconstructed by PAIR and PIDD, respectively. The estimated motion kernel by PIDD and motion phase recovered by PAIR are visualized as motion phase modulations  $\mathbf{P}$ .

### Note 5. Comparison study on DATASET IV (Patient DWI)

To further compare the performance on DATASET IV, we select 12 slices covering tumors and various brain tissues from 13 patient's data (Fig. S9). Significant motion artifacts (white arrows in Fig. S9) can be observed on some PAIR results, while PIDD can provide more robust performance on this patient dataset.

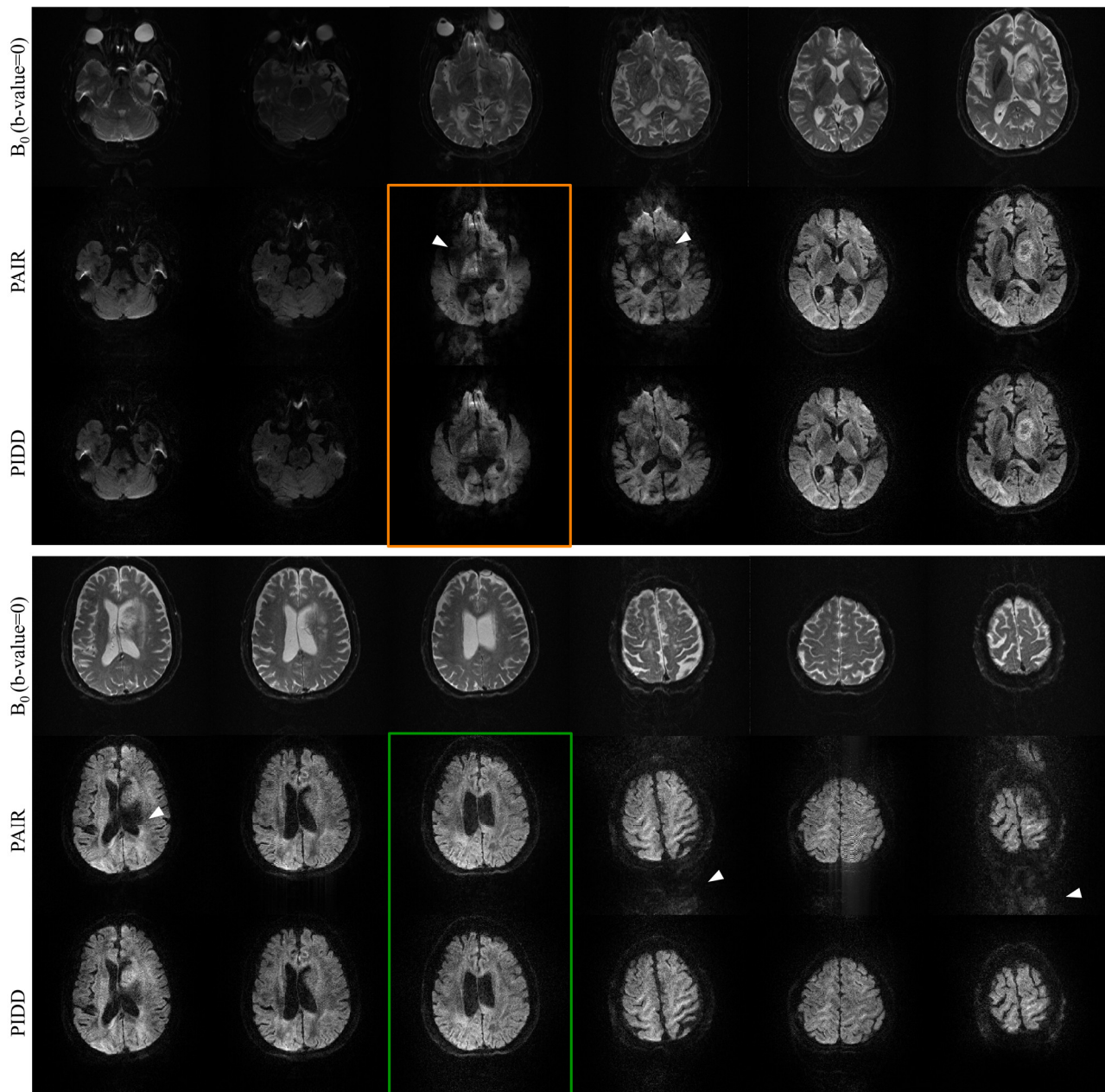


**Figure S9 | Comparison study on DATASET IV.** The b-value is  $1000 \text{ s/mm}^2$ . PAIR uses a set of optimized and fixed parameters to reconstruct all images, while PIDD is trained on the synthetic data. White arrows mark the artifacts.

---

## References

- 1 Mani, M., Jacob, M., Kelley, D. & Magnotta, V. Multi-shot sensitivity-encoded diffusion data recovery using structured low-rank matrix completion (MUSSELS). *Magnetic Resonance in Medicine*, 78, 494-507 (2017).
- 2 Qian, C. et al. A paired phase and magnitude reconstruction for advanced diffusion-weighted imaging. *IEEE Transactions on Biomedical Engineering*, DOI:10.1109/TBME.2023.3288031 (2023).
- 3 Cai, J.-F., Candès, E. J. & Shen, Z. A singular value thresholding algorithm for matrix completion. *SIAM Journal on Optimization*, 20, 1956-1982 (2010).
- 4 Haldar, J. P. Low-rank modeling of local k-space neighborhoods (LORAKS) for constrained MRI. *IEEE Transactions on Medical Imaging*, 33, 668-681 (2013).
- 5 Mani, M., Aggarwal, H. K., Magnotta, V. & Jacob, M. Improved MUSSELS reconstruction for high-resolution multi-shot diffusion weighted imaging. *Magnetic Resonance in Medicine*, 83, 2253-2263, (2020).
- 6 Aggarwal, H. K., Mani, M. P. & Jacob, M. MoDL-MUSSELS: model-based deep learning for multi-shot sensitivity-encoded diffusion MRI. *IEEE Transactions on Medical Imaging*, 39, 1268-1277 (2019).
- 7 Dai, L. et al. Learning from synthetic data for reference-free Nyquist ghost correction and parallel imaging reconstruction of echo planar imaging. *Medical Physics*, 50, 2135-2147 (2023).